International Journal of Multiphase Flow 35 (2009) 450–467

Contents lists available at ScienceDirect

International Journal of Multiphase Flow

journal homepage: www.elsevier.com/locate/ijmulflow

Dynamics of annular gas–liquid two-phase swirling jets

George A. Siamas, Xi Jiang *, Luiz C. Wrobel

Mechanical Engineering, School of Engineering and Design, Brunel University, Uxbridge UB8 3PH, UK

ARTICLE INFO

Article history:
Received 28 June 2008
Received in revised form 9 November 2008
Accepted 9 February 2009
Available online 20 February 2009

ABSTRACT

The dynamics of annular gas–liquid two-phase swirling jets have been examined by means of direct numerical simulation and proper orthogonal decomposition. An Eulerian approach with mixed-fluid treatment, combined with an adapted volume of fluid and a continuum surface force model, was used to describe the two-phase flow system. The unsteady, compressible, three-dimensional Navier–Stokes equations have been solved by using highly accurate numerical methods. Two computational cases have been performed to examine the effects of liquid-to-gas density ratio on the flow development. It was found that the higher density ratio case is more vortical with larger spatial distribution of the liquid, in agreement with linear theories. Proper orthogonal decomposition analysis revealed that more modes are of importance at the higher density ratio, indicating a more unstable flow field. In the lower density ratio case, both a central and a geometrical recirculation zone are captured while only one central recirculation zone is evident at the higher density ratio. The results also indicate the formation of a precessing vortex core at the high density ratio, indicating that the precessing vortex core development is dependent on the liquid-to-gas density ratio of the two-phase flow, apart from the swirl number alone.

1. Introduction

Gas–liquid two-phase jet flows are encountered in a variety of engineering applications such as in fuel injection, propulsion and combustion systems. The wide application of such flows has received much attention and various models to describe the liquid breakup have been proposed, but the exact mechanisms behind liquid breakup and atomization still remain unclear (De Villiers et al., 2004). Annular liquid jets are typically found in air-blasted and air-assisted atomisers which are integral parts in both aircraft propulsion systems and internal combustion engines (Gorokhovski and Hermann, 2008). Compared with round jets, an annular configuration can be advantageous in many applications due to the existence of thin liquid sheets, which can disintegrate much quicker, leading to a more effective atomisation. Annular jet flows are more complex compared to round jet flows due to the existence of two adjacent concentric shear layers near the jet nozzle exit, compared to one such shear layer in round jets. The annular configuration is responsible for the formation of a recirculation zone just after the nozzle exit (Siamas et al., 2008; Del Taglia et al., 2004; Sheen et al., 1996) which is a typical feature of annular jet flows.

In combustion and propulsion systems, the annular jet flow is usually swirled, since the introduction of swirling motion is regarded as an effective way to stabilize the flame near the burner exit (Gupta et al., 1984). Also, the introduction of swirl can result in a higher entrainment of the ambient fluid that can improve the flow mixing, especially in the shear-layer region (Hübner et al., 2003; Sheen et al., 1996). In atomization systems, the addition of swirl can speed-up the liquid disintegration and significantly alter the spray physics and characteristics (Liao et al., 2000). Detailed investigations on the physics of gas–liquid two-phase swirling jets are extremely limited. The existing studies on annular liquid jets were mainly based on experimental observations (Vanierschot and van den Bulck, 2007; Adzic et al., 2001; Ramamurthi and Tharakan, 1998; Sommerfeld and Qiu, 1991) and on simple mathematical formulations (Ibrahim and McKinney, 2006; Liao et al., 2000; Chuech, 1993). It is difficult to fully understand the liquid breakup mechanisms using theoretical and/or experimental approaches because of the complex interaction between the two phases.

An in-depth understanding of annular swirling gas–liquid two-phase jet flows can benefit atomiser design and potentially increase the efficiency of propulsion and combustion systems. In computational studies of such two-phase flows, the gas–liquid interface dynamics need to be realistically represented (Scardovelli and Zaleski, 1999). The traditional Reynolds-averaged Navier–Stokes (RANS) approach can lead to poor predictions of the unsteady dynamics of the flow due to the intrinsic time- or ensemble-averaging of the governing equations. The addition of swirl causes extra problems since the swirling motion cannot be easily modelled using RANS due to the effects of mean flow streamline curvature (Jakirlić et al., 2002). Large-eddy simulation can be utilized to overcome the problems associated with the RANS approach but it may not be sufficient to understand the detailed mechanisms in high-speed gas–liquid two-phase jet flows, as the small scales still

* Corresponding author. Tel.: +44 1895 266685: fax: +44 1895 256392.
E-mail address: Xi.Jiang@brunel.ac.uk (X. Jiang).

0301-9322/$ - see front matter © 2009 Elsevier Ltd. All rights reserved.
doi:10.1016/j.ijmultiphaseflow.2009.02.001

need to be modelled. The swirling motion can be captured using LES but only the major part of the turbulent motion is directly resolved (García-Villalba et al., 2006; García-Villalba and Fröhlich, 2006). In this perspective, direct numerical simulation (DNS) provides a powerful tool that not only increases the understanding on such complex multiphase flows, but also provides useful databases for the potential development of physical models for liquid breakup and atomization. DNS has been utilized by Ruith and Meiburg (2002) and Kollmann et al. (2001) to simulate vortex breakdown in single-phase swirling jets, but DNS of two-phase flows has been extremely scarce. Although DNS is very powerful the excessive computational cost needed to perform complex two-phase computations is always a drawback and therefore, for the time being, such simulations have to be restricted to relatively small flow regions such as those near the jet nozzle exit. DNS has been used to simulate the interface changes and turbulence in two-phase environments (Banerjee et al., 2004; Fulgosi et al., 2003; Lombardi et al., 1996) but the two phases were divided into two single-phase subdomains while the gas flow was considered to be incompressible. Klein (2005) performed DNS of a liquid sheet exhausting into a gaseous incompressible atmosphere under moderate Reynolds number. Direct computations of two-phase gas–liquid flows have been performed in axisymmetric and planar configurations (Siamas et al., 2008; Siamas and Jiang, 2007; Jiang and Siamas, 2007) and good agreement with linear theories has been obtained. However, the fine details of the flow vortical structure and mixing are not captured in idealized axisymmetric and planar simulations, due to the lack of three-dimensional vortex stretching and interaction. In addition, axisymmetric or planar simulations are not able to examine swirling effects. An extended study in full three dimensions is needed for detailed realization of the dynamics of the gas–liquid two-phase swirling flow.

This study aims at a better understanding of the flow physics of annular swirling gas–liquid two-phase jets. The effects of liquid-to-gas density ratio are examined. Variation of liquid-to-gas density ratio can be helpful in understanding the flow changes when injecting a different fuel or the same fuel under different conditions. Such changes can also be linked to the effects of Reynolds number on the flow physics. The study was based on DNS of two computational cases of annular gas–liquid two-phase swirling jets with different liquid-to-gas density ratios. The DNS results have been analyzed using the proper orthogonal decomposition (POD), also known in other fields as singular value decomposition and principal component analysis. POD is a low-dimensional analysis tool that can be used to examine coherent structures in fluid flow, which has not been extensively used to analyze two-phase swirling jets. In this study, the flow characteristics are examined by direct solution of the unsteady, non-dimensional Navier–Stokes equations using highly accurate numerical schemes. Fully three-dimensional (3D) parallel simulations have been performed. The flow fields are then analyzed using POD. In the following sections, governing equations and numerical methods used are presented followed by discussions on the results and the conclusions drawn.

2. Governing equations

The physical problem investigated is an annular swirling gas–liquid two-phase jet issuing into an ambient environment. The flow field concerned is the region above the nozzle exit plane. The flow field is described by the non-dimensional time-dependent Navier–Stokes equations in the Cartesian coordinate system (x,y,z), where the z-axis is aligned with the streamwise direction of the jet while the $x-y$ plane is the cross-streamwise direction. Reference quantities used in the normalization are the maximum streamwise velocity at the jet nozzle exit (computational domain inlet), the diameter of the annular jet (with radius measured from the middle of the annular sheet to the geometrical centre of the jet nozzle exit), the ambient temperature, gas density and viscosity and the liquid surface tension (assumed to be constant, resulting in a non-dimensional value of one). The non-dimensional quantities in the governing equations are: u, v, w: velocity components in x, y, z directions, respectively; t: time; γ: ratio of specific heats of the compressible gas; ρ: gas–liquid mixture density; ρ_g: gas density; ρ_l: liquid density (assumed constant); μ: gas–liquid mixture viscosity; μ_g: gas viscosity; μ_l: liquid viscosity (assumed constant); p: gas pressure; T: temperature; Y: liquid mass fraction; Φ: liquid volume fraction; κ: curvature; σ: surface tension; $E_T = \rho_g[e + (u^2 + v^2 + w^2)/2]$: total energy of the gas with e representing the internal energy per unit mass; Ma: Mach number; Pr: Prandtl number; Re: Reynolds number; Sc: Schmidt number; and We: Weber number.

The governing equations are formulated upon the conservation laws for mass, momentum and energy and they describe both phases in a single set of equations. In the Eulerian approach with mixed-fluid treatment adopted (Crowe, 2006), the two phases are assumed to be in local kinetic and thermal equilibrium, i.e. the relative velocities and temperatures are not significant, while the density and viscosity are considered as gas–liquid mixture properties. The Eulerian approach with mixed-fluid treatment is essentially a two-phase mean model, but it significantly simplifies the mathematical formulation for the two-phase flow thereby reduces the computational costs. In the current formulation only a non-reacting isothermal flow is considered, where the two phases exchange momentum only without phase change and energy transfer taking place. Thus $u_g = u_l = u$, $v_g = v_l = v$, $w_g = w_l = w$ and $T_g = T_l = T$. The non-dimensional governing equations can be written in a vector form as

$$\frac{\partial \boldsymbol{U}}{\partial t} + \frac{\partial \boldsymbol{E}}{\partial x} + \frac{\partial \boldsymbol{F}}{\partial y} + \frac{\partial \boldsymbol{G}}{\partial z} + \boldsymbol{H} = 0, \tag{1}$$

where the vectors $\boldsymbol{U}$, $\boldsymbol{E}$, $\boldsymbol{F}$, $\boldsymbol{G}$ and $\boldsymbol{H}$ are defined as

$$\boldsymbol{U} = \begin{pmatrix} \rho_g \\ \rho u \\ \rho v \\ \rho w \\ E_T \\ \rho Y \end{pmatrix},$$

$$\boldsymbol{E} = \begin{bmatrix} \rho_g u \\ \rho u^2 + p - \tau_{xx} \\ \rho u v - \tau_{xy} \\ \rho u w - \tau_{xz} \\ (E_T + p)u + q_x - u\tau_{xx,g} - v\tau_{xy,g} - w\tau_{xz,g} \\ \rho u Y - \frac{1}{ReSc}\left(\mu \frac{\partial Y}{\partial x}\right) \end{bmatrix},$$

$$\boldsymbol{F} = \begin{bmatrix} \rho_g v \\ \rho u v - \tau_{xy} \\ \rho v^2 + p - \tau_{yy} \\ \rho u w - \tau_{yz} \\ (E_T + p)v + q_y - u\tau_{xy,g} - v\tau_{yy,g} - w\tau_{yz,g} \\ \rho v Y - \frac{1}{ReSc}\left(\mu \frac{\partial Y}{\partial y}\right) \end{bmatrix},$$

$$\boldsymbol{G} = \begin{bmatrix} \rho_g w \\ \rho u w - \tau_{xz} \\ \rho v w - \tau_{yz} \\ \rho w^2 + p - \tau_{zz} \\ (E_T + p)w + q_z - u\tau_{xz,g} - v\tau_{yz,g} - w\tau_{zz,g} \\ \rho w Y - \frac{1}{ReSc}\left(\mu \frac{\partial Y}{\partial z}\right) \end{bmatrix},$$

$$\boldsymbol{H} = \begin{pmatrix} 0 \\ -\frac{\sigma\kappa}{We}\frac{\partial\Phi}{\partial x} \\ -\frac{\sigma\kappa}{We}\frac{\partial\Phi}{\partial y} \\ -\frac{\sigma\kappa}{We}\frac{\partial\Phi}{\partial z} \\ 0 \\ 0 \end{pmatrix}. \tag{2}$$

The constitutive relations for viscous stress and heat flux components are given in Table 1. Assuming the gas medium as an ideal gas, the governing equations for the gas–liquid two-phase flow system include also the perfect gas law, given by

$$p = \frac{\rho_g T}{\gamma Ma^2}. \tag{3}$$

The physics of the gas–liquid flow system is computed and analyzed using the volume of fluid (VOF) method by Hirt and Nichols (1981), which employs the liquid volume fraction. The liquid volume fraction works as an indicator to identify the different fluids. A liquid volume fraction value of one, $\Phi = 1$, corresponds to pure liquid and a value of zero, $\Phi = 0$, corresponds to pure gas. In between the two values, $0 < \Phi < 1$, a gas–liquid interface region exists and the fluid is considered as a mixture. The VOF method is commonly used to model multiphase flow problems since the volume fluxes can be formulated algebraically without the need of an exact interface reconstruction (Rider and Kothe, 1998). In this study, the original VOF method has been adapted to solve an equation for the liquid mass fraction Y rather than the volume fraction Φ in order to suit the compressible gas phase formulation (Siamas et al., 2008; Siamas and Jiang, 2007; Jiang and Siamas, 2007). From their definitions, a relation between liquid volume fraction and liquid mass fraction can be derived as

$$\Phi = \frac{\rho_g Y}{\rho_l - (\rho_l - \rho_g)Y}. \tag{4}$$

Following Gueyffier et al. (1999), the density and viscosity of the gas–liquid two-phase fluid flow are considered as functions of the liquid volume fraction and densities and viscosities of both phases, given by

$$\rho = \Phi\rho_l + (1-\Phi)\rho_g, \tag{5}$$

$$\mu = \Phi\mu_l + (1-\Phi)\mu_g. \tag{6}$$

Eqs. (5) and (6) are utilized in conjunction with the VOF method, to account for the contributions of the two individual phases to the mixture properties.

The gas–liquid interface dynamics are resolved using a continuum surface force (CSF) model developed by Brackbill et al. (1992), which represents the surface tension effect as a continuous volumetric force acting within the region where the two phases coexist. The CSF model overcomes the problem of directly computing the surface tension integral that appears in the Navier–Stokes momentum equations, which requires the exact shape and location of the interface. In the CSF model, the surface tension force in its non-dimensional form, as it appears in Eq. (2), can be approximated as $\sigma\kappa/We\nabla\Phi$, with the curvature of the interface given by

$$\kappa = -\nabla\cdot\left(\frac{1}{|\nabla\Phi|}\nabla\Phi\right). \tag{7}$$

Table 1
The constitutive relations for viscous stress and heat flux components.

Gas–liquid mixture	Gas
$\tau_{xx} = -\frac{2}{3}\frac{\mu}{Re}\left(-2\frac{\partial u}{\partial x}+\frac{\partial v}{\partial y}+\frac{\partial w}{\partial z}\right)$	$\tau_{xx,g} = -\frac{2}{3}\frac{\mu_g}{Re}\left(-2\frac{\partial u}{\partial x}+\frac{\partial v}{\partial y}+\frac{\partial w}{\partial z}\right)$
$\tau_{xy} = \frac{\mu}{Re}\left(\frac{\partial v}{\partial x}+\frac{\partial u}{\partial y}\right)$	$\tau_{xy,g} = \frac{\mu_g}{Re}\left(\frac{\partial v}{\partial x}+\frac{\partial u}{\partial y}\right)$
$\tau_{xz} = \frac{\mu}{Re}\left(\frac{\partial w}{\partial x}+\frac{\partial u}{\partial z}\right)$	$\tau_{xz,g} = \frac{\mu_g}{Re}\left(\frac{\partial w}{\partial x}+\frac{\partial u}{\partial z}\right)$
$\tau_{yy} = -\frac{2}{3}\frac{\mu}{Re}\left(\frac{\partial u}{\partial x}-2\frac{\partial v}{\partial y}+\frac{\partial w}{\partial z}\right)$	$\tau_{yy,g} = -\frac{2}{3}\frac{\mu_g}{Re}\left(\frac{\partial u}{\partial x}-2\frac{\partial v}{\partial y}+\frac{\partial w}{\partial z}\right)$
$\tau_{yz} = \frac{\mu}{Re}\left(\frac{\partial w}{\partial y}+\frac{\partial v}{\partial z}\right)$	$\tau_{yz,g} = \frac{\mu_g}{Re}\left(\frac{\partial w}{\partial y}+\frac{\partial v}{\partial z}\right)$
$\tau_{zz} = -\frac{2}{3}\frac{\mu}{Re}\left(\frac{\partial u}{\partial x}+\frac{\partial v}{\partial y}-2\frac{\partial w}{\partial z}\right)$	$\tau_{zz,g} = -\frac{2}{3}\frac{\mu_g}{Re}\left(\frac{\partial u}{\partial x}+\frac{\partial v}{\partial y}-2\frac{\partial w}{\partial z}\right)$
	$q_x = \frac{-\mu_g}{(\gamma-1)Ma^2PrRe}\frac{\partial T}{\partial x}$
	$q_y = \frac{-\mu_g}{(\gamma-1)Ma^2PrRe}\frac{\partial T}{\partial y}$
	$q_z = \frac{-\mu_g}{(\gamma-1)Ma^2PrRe}\frac{\partial T}{\partial z}$

3. Numerical methods

3.1. Time advancement and spatial discretisation

The numerical methods include the high-order finite-difference schemes for spatial discretization and time advancement. The governing equations are integrated forward in time using a third-order compact-storage fully explicit Runge–Kutta scheme (Williamson, 1980). The solution variables $(\rho_g, \rho u, \rho v, \rho w, E_T, \rho Y)$ in Eq. (2) are advanced in time using a three-step compact-storage third-order Runge–Kutta scheme of the family derived by Wray (1986). Two storage locations are employed for each time-dependent variable and at each sub-step at these locations, say Q_1 and Q_2 with Q representing the solution variables, are updated simultaneously as follows:

$$Q_1^{new} = a_1 Q_1^{old}\Delta t + Q_2^{old}, \quad Q_2^{new} = a_2 Q_1^{old}\Delta t + Q_2^{old}. \tag{8}$$

The constants (a_1, a_2) in Eq. (8) are chosen to be (2/3,1/4) for sub-step 1, (5/12,3/20) for sub-step 2 and (3/5,3/5) for sub-step 3. At the beginning of each full time step, Q_1 and Q_2 are equal. The data in Q_1 is used to compute $\partial\boldsymbol{U}/\partial t$ in Eq. (1). The computed $\partial\boldsymbol{U}/\partial t$ is stored in Q_1 to save storage (overwriting the old Q_1). Eq. (8) is then used to update Q_1 and Q_2. In Eq. (8), Δt is the time step, which is limited by the Courant–Friedrichs–Lewy condition for stability.

During the time advancement, the density and viscosity of the gas–liquid two-phase flow system are calculated according to Eqs. (5) and (6), using the volume fraction Φ calculated from Eq. (4). However, the liquid mass fraction Y in Eq. (4) needs to be calculated from the solution variable ρY first. Using q to represent ρY at each time step, the liquid mass fraction Y can be calculated as

$$Y = \frac{\rho_l q}{\rho_l\rho_g + (\rho_l - \rho_g)q}. \tag{9}$$

Eq. (9) can be derived from Eqs. (4) and (5). At each time step, Eq. (9) is used first to calculate the liquid mass fraction, Eq. (4) is then used to calculate the liquid volume fraction and Eqs. (5) and (6) are finally used to update the mixture density and viscosity.

Spatial differentiation is achieved using the sixth-order compact (*Padé*) finite-difference scheme of Lele (1992), which has been widely used in DNS of fluid flow problems. Solutions for the discretized equations are obtained by solving the tridiagonal system of equations.

3.2. Boundary conditions

The 3D computational domain is bounded by the inflow and the outflow boundaries in the streamwise direction and open boundaries with the ambient field in the jet radial (cross-streamwise) direction. The non-reflecting characteristic boundary conditions due to Thompson (1987) are applied at the open boundaries, which prevent the wave reflections from the outside of the computational domain. The non-reflecting boundary conditions are also used at

the outflow boundary in the streamwise direction. The spurious wave reflections from outside the boundary have been controlled by using a sponge layer ($L_{zs} < z \leqslant L_z$) next to the outflow boundary (Jiang and Luo, 2000), which has been proved to be very effective in controlling the wave reflections through the outflow boundary. The results of the sponge layer are unphysical and therefore are not used in the data analysis.

The inflow conditions at the jet nozzle exit need careful attention. They represent the initial mass and momentum distributions of the annular gas–liquid two-phase jet. Under swirling conditions, they must be able to represent the amount of swirl at the jet nozzle exit as realistically as possible. Based on the concept of Pierce and Moin (1998) for numerical generation of equilibrium swirling inflow conditions, analytical solutions of the axial and azimuthal velocity components were derived, which enable simple and precise specification of the desired swirl level (Jiang et al., 2008a). The analytical profiles of axial and azimuthal velocities are given as

$$w = -\frac{1}{4}\frac{f_x}{\mu}\left(r^2 - \frac{R_i^2 - R_o^2}{\ln R_i - \ln R_o}\ln r + \frac{R_i^2 \ln R_o - R_o^2 \ln R_i}{\ln R_i - \ln R_o}\right),$$
$$u_\theta = -\frac{1}{3}\frac{f_\theta}{\mu}\left(r^2 - \frac{R_i^2 + R_i R_o + R_o^2}{R_i + R_o}r + \frac{R_i^2 R_o^2}{R_i + R_o}\frac{1}{r}\right), \tag{10}$$

where $r = \sqrt{(x - x_0)^2 + (y - y_0)^2}$ is the radial distance, R_i and R_o are the inner and outer radii of the annular jet, respectively. In Eq. (10) f_x and f_θ can be defined by the maximum velocities at the inflow boundary. For a unit maximum velocity, which is often the case when a non-dimensional form of the governing equations is employed, the constant f_x is defined as

$$f_x = -\frac{8\mu(\ln R_o - \ln R_i)}{R_o^2 - R_i^2 + R_i^2 \ln\left[\frac{R_i^2 - R_o^2}{2(\ln R_i - \ln R_o)}\right] - R_o^2 \ln\left[\frac{R_i^2 - R_o^2}{2(\ln R_i - \ln R_o)}\right] - 2R_i^2 \ln R_o + 2R_o^2 \ln R_i}. \tag{11}$$

The parameter f_θ defines the degree of swirl. For known w and u_θ the swirl number can be calculated from

$$S = \frac{\int_{R_i}^{R_o} w u_\theta r^2\, dr}{R_o \int_{R_i}^{R_o} w^2 r\, dr}. \tag{12}$$

A certain swirl number can be conveniently achieved by adjusting the constant f_θ in Eq. (10). From the azimuthal velocity u_θ, the cross-streamwise velocity components at the inflow can be specified by $u = -u_\theta y/r$ and $v = u_\theta x/r$. At the inflow boundary, the liquid mass fraction profile has been specified using a distribution similar to the streamwise (axial) velocity profile.

The mean velocity at the inflow was perturbed by a flapping mode which contains two helical modes with the same frequency and amplitude (Uchiyama, 2004). The velocity components at the jet nozzle exit $z = 0$ can be given as

$$u = \bar{u} + A\sin(m\varphi - 2\pi f_0 t), \quad v = \bar{v} + A\sin(m\varphi - 2\pi f_0 t),$$
$$w = \bar{w} + A\sin(m\varphi - 2\pi f_0 t), \tag{13}$$

where A is the amplitude of disturbance, m is the mode number, φ is the azimuthal angle and f_0 the excitation frequency. The amplitude of the disturbance is 1% of the maximum value of the streamwise velocity. The non-dimensional frequency (Strouhal number) of the unsteady disturbance is chosen to be $f_0 = 0.3$, which is the most unstable mode leading to the jet preferred mode of instability (Hussain and Zaman, 1981). Two helical disturbances of $m = 1$ and $m = -1$ were superimposed on the temporal disturbance (Uchiyama, 2004). For the flow configuration under investigation, both absolute instability and convective instability can exist under certain flow conditions (Shen and Li, 2001). From an application point of view, the topology of the flow vortical structures may be of greater importance, which will be discussed later in the results and discussion.

4. Computational details and proper orthogonal decomposition

4.1. Computational parameters

Two computational cases have been performed in order to investigate the effects of liquid-to-gas density ratio on the flow development of an annular gas–liquid two-phase jet: Case A with $\rho_l/\rho_g = 2.5$ and Case B with $\rho_l/\rho_g = 5.0$. The input parameters of Case B correspond to diesel injection into compressed air at approximately 15 MPa and 300 K (Perry and Green, 1998). In Case A, the density ratio was halved to examine its effects on the flow. The liquid surface tension is about 0.025 N/m. The width of the annular sheet is 0.35 while the thickness of the liquid sheet is 0.2 and it is located in the middle of the annulus. Using the reference quantities defined in Section 2, the input parameters used in the simulations are (Perry and Green, 1998): Mach number $Ma = 0.4$; Reynolds number $Re = 2000$; Prandtl number $Pr = 0.76$; Schmidt number $Sc = 0.76$; Weber number $We = 240$; swirl number $S = 0.4$ and ratio of specific heats $\gamma = 1.64$.

The excessive computational cost needed to perform complex two-phase DNS limits the computation to regions close to the jet nozzle exit. The dimensions of the computational box used are $L_x = L_y = L_z = 10$. The grid system is of $512 \times 512 \times 512$ nodes with a uniform distribution in each direction. The grid determines the scales that are resolved while the resolution must be sufficient to capture the smallest scales. The Kolmogorov length scale is commonly quoted as the smallest scale that needs to be resolved in DNS-type simulations and can be defined as (Freitag and Klein, 2005) $\eta_K = L^*_{ref}/Re_t^{3/4}$, where L^*_{ref} is the dimensional reference length scale and Re_t is the turbulent Reynolds number. The L^*_{ref} corresponding to the nominal Reynolds and Mach numbers is around 2 μm for the simulations performed. Based on the non-dimensional input parameters and the velocity fluctuations observed in the flow fields, the smallest Kolmogorov length scale η_K can be estimated to be around 0.3 μm, which is larger than the grid spacing η_{grid} of around 0.04 μm. Therefore, the grid resolution was sufficient to capture the smallest scales. The physical scales of the problem corresponding to the non-dimensional parameters used are very small. However, tests showed that changing the Mach number from 0.4 to 0.05 did not lead to appreciable changes in the solution, indicating that the DNS results may be applicable for physical problems that are 10 times larger than that indicated by the L^*_{ref}. The scaled-up physical scales correspond to those of micro-diesel injector nozzles (Baik et al., 2003) and microelectromechanical nozzles (Wang and Li, 2004). Although scaling to larger configurations can be approximate or even distorted, DNS results of this type can be used to gain better insights into practical problems. Under this perspective the results presented in this study are considered to be useful for understanding fuel injection processes in practical applications.

Parallel computations have been performed, under the message passing interface environment, on an IBM pSeries 690 Turbo Supercomputer HPCx utilizing 512 processors. Each simulation case costs around 300,000 Allocation Units on HPCx. The 3D parallel DNS code used in this study was developed from the 3D parallel DNS code for gas jets (Jiang et al., 2007; Jiang and Luo, 2003) based on the gas–liquid two-phase flow formulation used in the axisymmetric and planar simulations (Siamas et al., 2008; Siamas and Jiang, 2007; Jiang and Siamas, 2007). The results presented herein are considered to be grid and time-step independent and are discussed in terms of the instantaneous and time-averaged flow properties. The DNS results have also been analyzed using POD.

4.2. Proper orthogonal decomposition

As a powerful tool to investigate the mode effects in vortical flow fields and turbulence, POD is used to analyze the flow data generated by the DNS. The principle of POD is the decomposition of the flow field into a weighted linear sum of orthogonal eigenfunctions. The coherent structures in the flow field are described by the eigenfunctions of the two-point correlation tensor. The POD hypothesis is that different types of coherent motion that may occur within the flow will give rise to different POD eigenfunctions. The largest eigenvalue corresponds to the structure with most energy (Gunes and Rist,2007, 2004). The method of snapshots (Holmes et al., 1998; Sirovich, 1987) is utilized in this work to solve the associated eigenvalue problem.

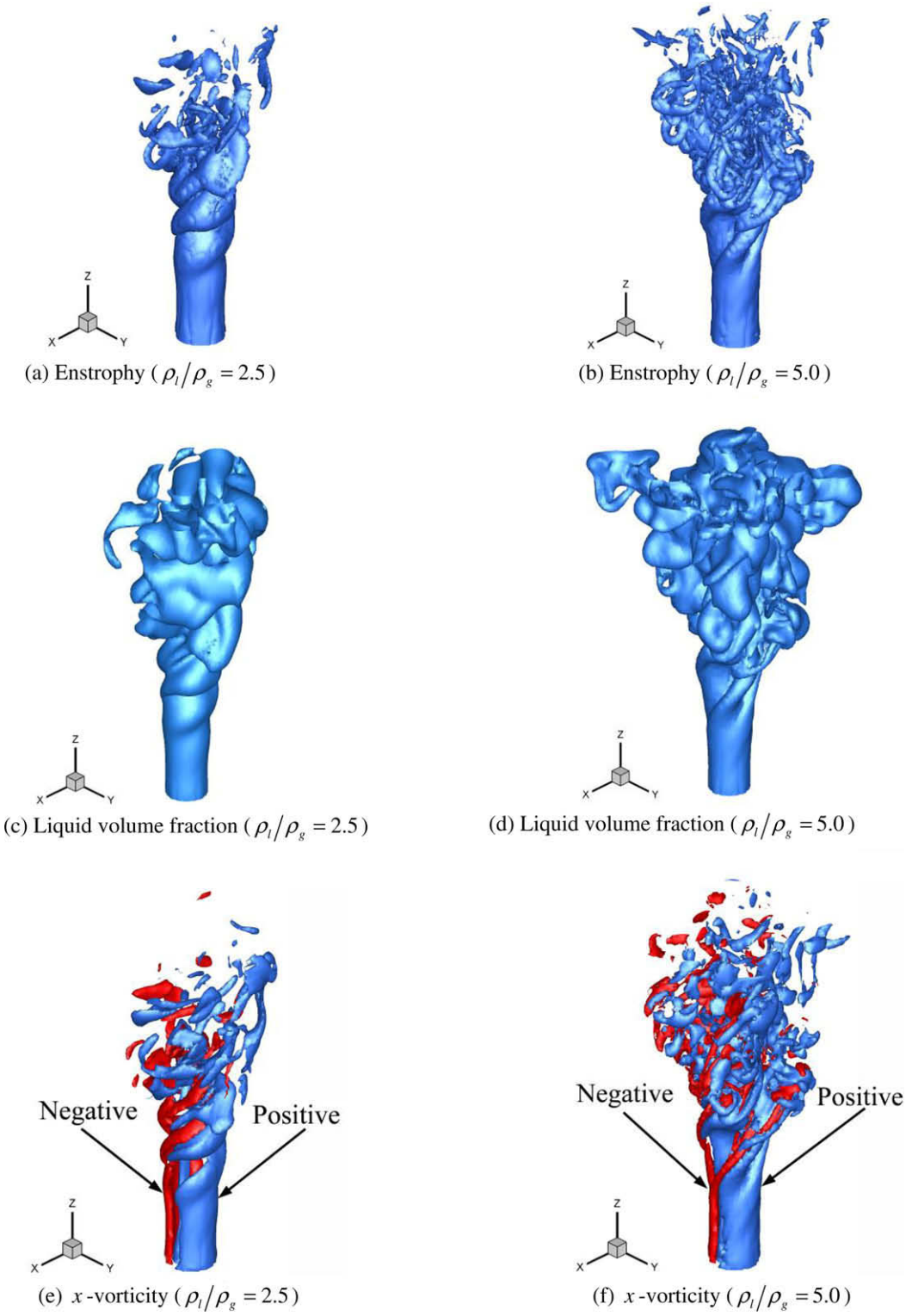

(a) Enstrophy ($\rho_l/\rho_g = 2.5$)

(b) Enstrophy ($\rho_l/\rho_g = 5.0$)

(c) Liquid volume fraction ($\rho_l/\rho_g = 2.5$)

(d) Liquid volume fraction ($\rho_l/\rho_g = 5.0$)

(e) x-vorticity ($\rho_l/\rho_g = 2.5$)

(f) x-vorticity ($\rho_l/\rho_g = 5.0$)

Fig. 1. Instantaneous isosurfaces of enstrophy, liquid volume fraction and x-vorticity at $t = 33.3$.

In this method, an ensemble of M discrete instantaneous flow variables $\zeta(\vec{x}, t_k)$ (velocity fields in this study) acquired at time instants $t_k (k = 1,2,\ldots,M)$ is considered in a two-dimensional (2D) slice A of the 3D computational domain. The POD analysis is performed primarily in 2D slices along the streamwise direction ($z = 2.0, 4.0, 6.0, 8.0$) to avoid the excessive computer memory requirements of a full 3D POD analysis of the DNS datasets. The full grid resolution of the DNS data is used. Due to the excessive requirements on computer memory resources (RAM, virtual memory), a direct 3D POD analysis was not performed which would require a significant amount of data storage for the 3D flow field history data, involving at least hundreds of snapshots

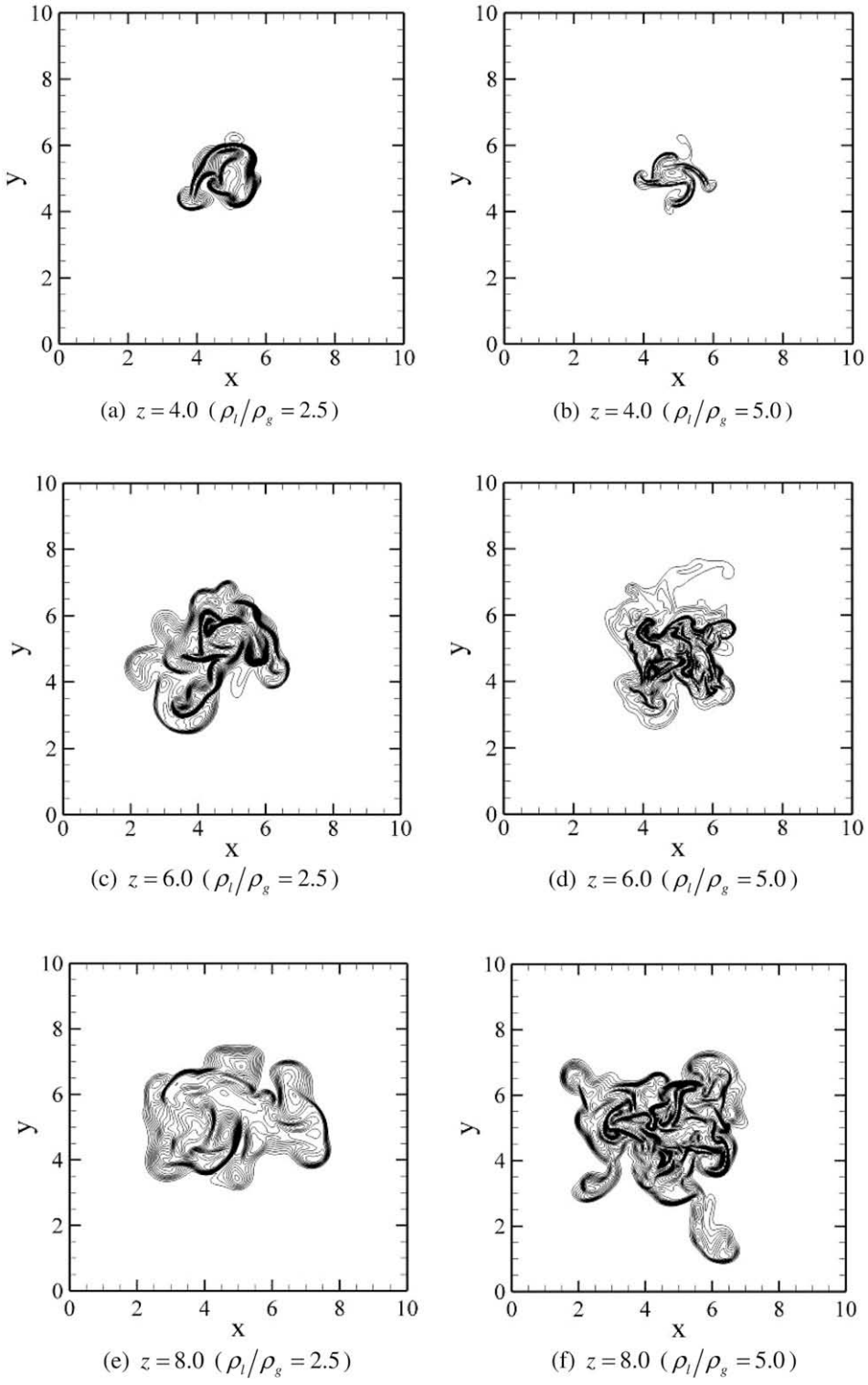

Fig. 2. Instantaneous liquid volume fraction contours in various streamwise planes at $t = 33.3$.

of the results on the 512^3 grid. In addition, the POD data post processing involves massive matrix operations, incurring excessive memory and storage requirements for the 3D history data. In the meantime, POD analysis of individual 2D sections can provide adequate information on the modal effects in a particular location or cross-section of the flow field, while 3D POD can only provide the overall modal effects. In performing the POD analysis, the time-average of the velocity field is computed and a new set of measurements $\xi(\vec{x},t)$, which is the fluctuating velocity field, is calculated as follows:

$$\bar{\zeta}(\vec{x}) = \frac{1}{M}\sum_{k=1}^{M}\zeta(\vec{x},t_k) \quad \text{and} \quad \xi(\vec{x},t_k) = \zeta(\vec{x},t_k) - \bar{\zeta}(\vec{x}). \tag{14}$$

A two-point correlation matrix $\boldsymbol{C}$ can be constructed as

$$C_{ij} = \frac{1}{M}\int_A \xi(\vec{x},t_i)\xi(\vec{x},t_j)\,d\vec{x}, \quad \text{where} \quad (i,j = 1,2,\ldots,M). \tag{15}$$

The eigenvectors $\vec{a}_k^n$ and their corresponding eigenvalues λ_k can be found from the numerical solution of the equation

$$\boldsymbol{C}\vec{a}_k^n = \lambda_k\vec{a}_k^n, \quad \text{where} \quad (k,n = 1,2,\ldots,M). \tag{16}$$

Using the eigenvectors $\vec{a}_k^n$ of matrix $\boldsymbol{C}$, POD eigenfunctions $\phi^n(\vec{x})$ at mode n, which are optimal for the representation of the corresponding DNS data, can be linearly constructed by combining the fluctuating velocity as

$$\phi^n(\vec{x}) = \sum_{k=1}^{M}\vec{a}_k^n\xi(\vec{x},t_k). \tag{17}$$

The POD eigenfunctions are orthogonal while the eigenvalues are positive $(\lambda_k \geq 0)$ in descending order $(\lambda_k > \lambda_{k+1})$, where $(k = 1,2,\ldots,M)$. Each eigenvalue quantifies the kinetic energy of the flow field datasets. The average fluctuating energy in the datasets can be calculated by summing up all the eigenvalues, $E = \sum_{k=1}^{M}\lambda_k$.

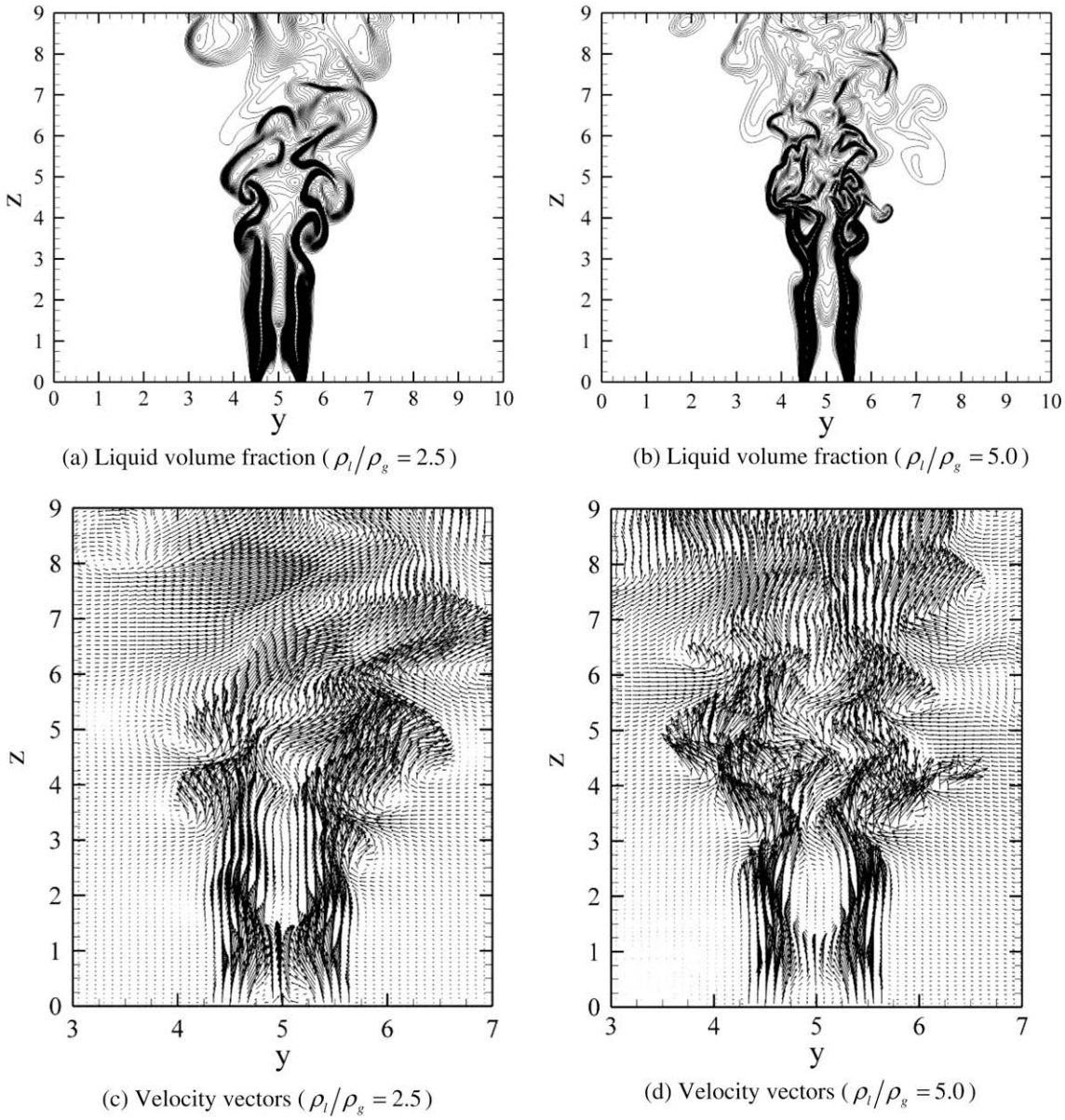

Fig. 3. Instantaneous liquid volume fraction contours and velocity vectors in $x = 5.0$ plane at $t = 33.3$.

The POD eigenfunctions can then be used to reconstruct the velocity fields as

$$\tilde{\xi}(\vec{x},t) = \sum_{n=1}^{N} \vec{a}_k^n \phi^n(\vec{x}), \tag{18}$$

where N is the number of POD modes to be used for the reconstruction. Eq. (18) is known as the "POD reconstruction formula". In general the first few modes capture most of the energy of the flow as quantified by the λ_k values. In other words, $N \ll M$ for flow reconstruction of large datasets using POD.

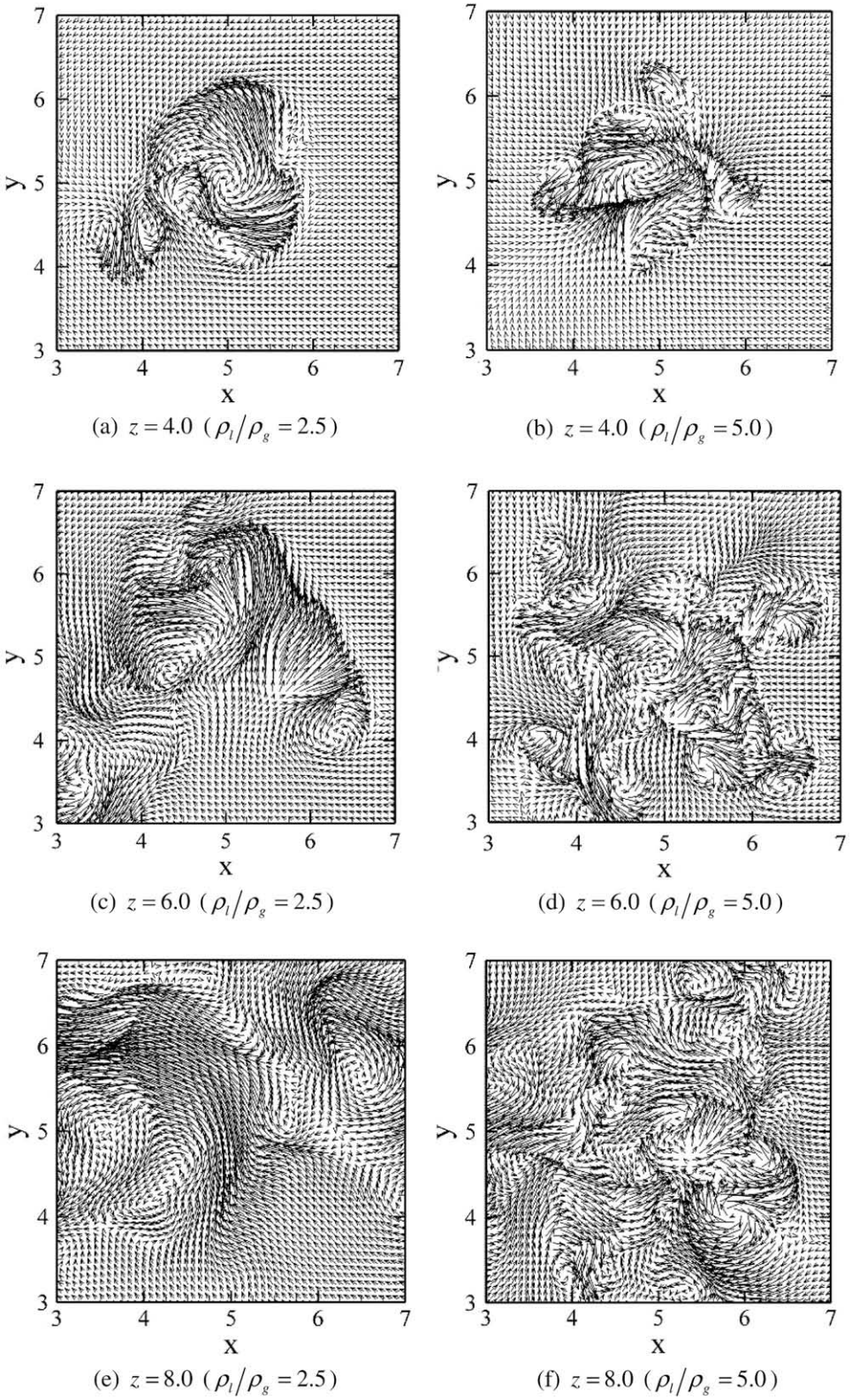

Fig. 4. Instantaneous velocity vector maps in various streamwise planes at $t = 33.3$.

5. Results and discussion

5.1. Instantaneous flow properties

The instantaneous isosurfaces of enstrophy $\Omega = (\omega_x^2 + \omega_y^2 + \omega_z^2)/2$, liquid volume fraction Φ and x-vorticity ω_x at $t = 33.3$ are shown in Fig. 1. The individual vorticity components are defined as $\omega_x = \partial w/\partial y - \partial v/\partial z$, $\omega_y = \partial u/\partial z - \partial w/\partial x$ and $\omega_z = \partial v/\partial x - \partial u/\partial y$. From Fig. 1, it is clear that the flow field is dominated by large-scale vortical structures due to the Kelvin–Helmholtz type shear layer instability. In 3D configurations, streamwise vorticity is generated by 3D vortex stretching and interaction, a feature absent in idealized

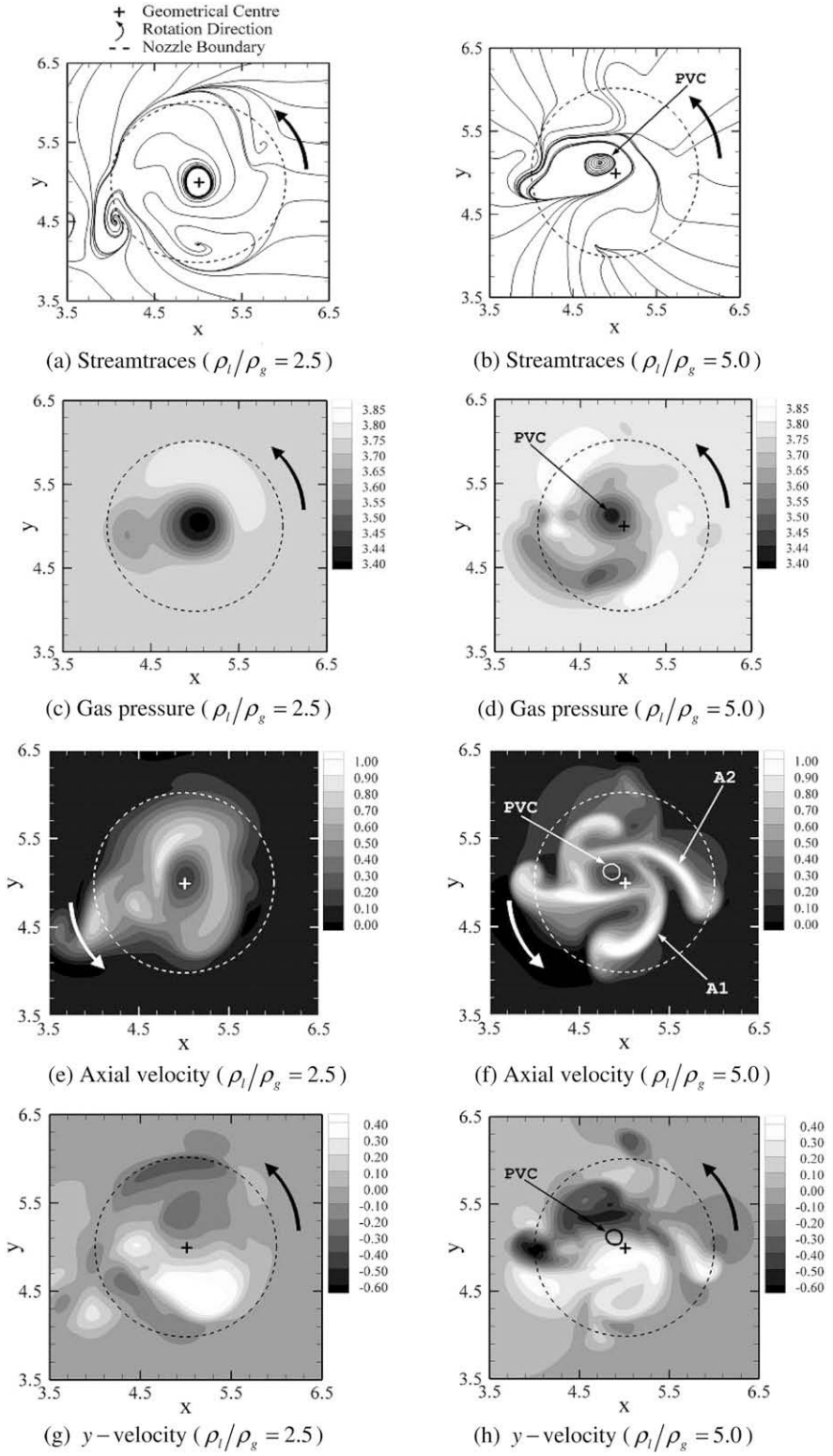

Fig. 5. Instantaneous streamtraces, gas pressure, axial velocity (w) and $y-$velocity (v) in $z = 4.0$ plane at $t = 33.3$.

axisymmetric and planar configurations. The presence of streamwise and cross-streamwise vorticity affects the liquid dispersion as shown in Fig. 1(c) and (d). In both cases the liquid dispersion shows increasing trends as the flow progresses from upstream to further downstream locations, forming a conical shape. This is largely due to the swirling nature of the jet. It is noticed that there is no formation of significant vortices at upstream locations, and the formation of vortices at the downstream locations is a consequence of the spatial development of the flow due to the growth of the Kelvin–Helmholtz instability. In Fig. 1, it is evident that Case B ($\rho_l/\rho_g = 5.0$) is more vortical than Case A ($\rho_l/\rho_g = 2.5$), causing the jet to form smaller vortical structures, particularly at the

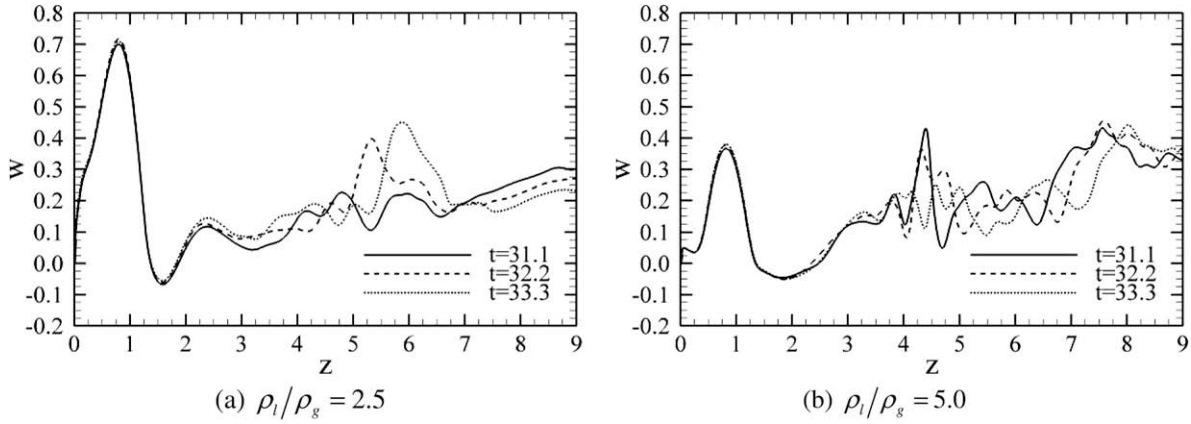

Fig. 6. Instantaneous streamwise velocity profiles at the jet centreline at different time instants.

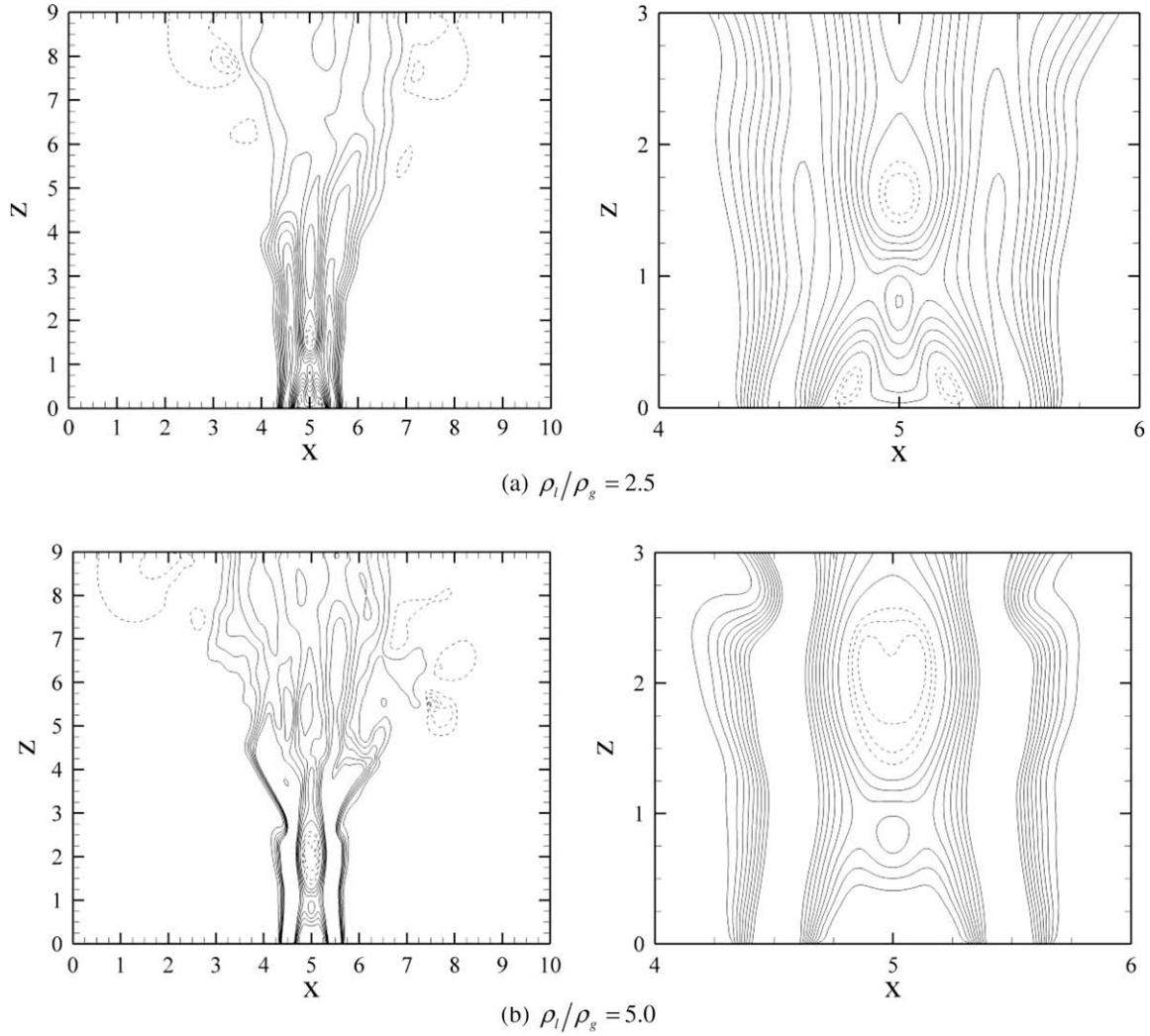

Fig. 7. Time-averaged streamwise velocity contours in $y = 5.0$ plane (solid line: positive; dashed line: negative).

downstream. This trend is consistent with the observations of Lin (2003), Shen and Li (1996a) and Rangel and Sirignano (1988). It is worth mentioning that in cases where the jet is assumed to be inviscid (Shen and Li, 1996b), a reduced liquid-to-gas density ratio, shows promoting instability characteristics, compared to demoting instability trends found in viscous jet flows. By comparing Fig. 1(c) and (d) it is clear that doubling the liquid-to-gas density ratio increases the cross-streamwise dispersion of the liquid. Fig. 1(e) and (f) show the instantaneous isosurfaces of the x-vorticity component for both cases. It is noticed that both negative and positive vorticity is present. This is an indication of the complex vortices, a feature which is associated with the two adjacent shear layers in the annular configuration.

To further clarify the liquid distribution, Fig. 2 shows the instantaneous liquid volume fraction contours in various streamwise planes. In both cases the liquid dispersion is increased at progressively downstream locations. The instantaneous liquid spatial distribution is quite complex with Case B ($\rho_l/\rho_g = 5.0$) showing a helical liquid distribution, while the liquid distribution in Case A ($\rho_l/\rho_g = 2.5$) is smoother. Further downstream, in both cases, the liquid distribution grows in the cross-streamwise directions, indicating larger spreading. At the downstream location $z = 8.0$, Case B shows larger liquid spreading, as it was also shown in Fig. 1(d). In Fig. 2, it is also noticed that Case A shows smoother spatial liquid distributions, due to the stabilizing effects of the lower liquid-to-gas density ratio. The increased instability observed in Case B causes sharp and sudden liquid topology changes as shown in Fig. 2(d) and (f).

The instantaneous liquid volume fraction contours and velocity vectors in $x = 5.0$ plane at $t = 33.3$ are shown in Fig. 3. Consistent with the observations in Fig. 1(c) and (d), Case B shows wider liquid dispersion. The reduced liquid-to-gas density ratio limits the cross-streamwise liquid distribution as it was also noticed in idealized axisymmetric non-swirling simulations (Siamas et al., 2008). An interesting feature in Fig. 3(a) is that the bell-shaped envelope within the annulus just above the jet nozzle exit is smaller than that in Fig. 3(b). This can be due to the presence of a geometrical recirculation zone (GRZ), which is formed adjacent to the nozzle exit and can bring the liquid back to region near the nozzle exit, a common feature of annular jet flows (Sheen et al., 1996). For Case B, however, the envelope is more elongated without much liquid present inside it. A close examination of Fig. 3(c) and (d) revealed that Case B is more vortical, consistent with the observations in Fig. 1, indicating that the increased liquid-to-gas density ratio promotes the Kelvin–Helmholtz instability. Both cases develop vortical structures after $z = 3.0$ in the streamwise direction, which are highly inhomogeneous with large spatial changes. In both cases, a more uniform velocity field is present after $z = 6.0$ where no obvious large-scale vortical structures can be seen, indicating that some large vortical structures might have broken down into smaller scales at downstream locations. It is worth noticing that the liquid volume fraction in Figs. 2 and 3 appears to be spread, which is mainly because the interface reconstruction was not performed in this study. The other reason for the spread liquid distribution is that the flow domain is very close to the jet nozzle exit where the liquid breakup and ligament formation are not prevalent.

Fig. 4 shows the instantaneous velocity vector maps in various streamwise planes at $t = 33.3$. For clarity, the vector plots are only shown for a limited number of grid points. Both cases show complex vortical structures at the downstream locations. The vortical structures are developed due to the Kelvin–Helmholtz instability which is triggered by the external perturbation supplied at the inlet. At $z = 4.0$ Case A shows a flow pattern that is largely affected by the external swirl, and the flow field appears to be more stable with fewer local rotating patterns. Case B shows very complex structures, particularly in planes $z = 6.0$ and $z = 8.0$, where the large vortical structures have collapsed to smaller ones, consistent with the observations in Fig. 1(b). Case A is less vortical where no significant small-scale structures are evident in $z = 6.0$ and $z = 8.0$, since the reduced liquid-to-gas density ratio demotes the instability characteristics. The tendency found herein is in good agreement with linear theories regarding the liquid-to-gas density ratio instability effects (Lin, 2003; Shen and Li, 1996a; Rangel and Sirignano, 1988). The higher density ratio case has more fine vortical structures than the lower density ratio case. The results indicate that the flow is more unstable at high density ratios, which is the fluid dynamic behaviour of higher Reynolds number flows.

Instantaneous contours of gas pressure, axial velocity (w), $y-$ velocity (v) and streamtraces in $z = 4.0$ plane at $t = 33.3$ are presented in Fig. 5 for both computational cases. In Fig. 5(b) an inner rotating structure can be observed very close to the nozzle geometrical centre, which is known as the precessing vortex core (PVC) (Gupta et al., 1984). The centre of the PVC is located at around ($x = 4.85$, $y = 5.15$) at this time instant. It is very important to notice that there is no PVC development in Case A. This is due to the fact that the higher density ratio case has a higher azimuthal momentum flux, leading to more significant swirling effects. It is known that the PVC can only develop in swirling jets, but its exact mechanisms and the factors affecting its presence are still unclear (Syred, 2006; Lucca-Negro and O'Doherty, 2001). The LES results of García-Villalba and Fröhlich (2006) showed that the PVC is mainly associated with high swirl number flows and a PVC was not observed in low swirl number jet flows ($S < 0.55$). This was noticed for swirling round jets (Syred, 2006; Gupta et al., 1984). In this study the swirl number is less than 0.55, but the PVC is formed in Case B as shown in Fig. 5(b). This is likely associated with the gas–liquid two-phase flow investigated herein. In Case A the flow does not allow the PVC development, however the PVC develops in Case B due to the higher azimuthal momentum flux in this case. Thus, the PVC development in two-phase flows depends not only on the swirl number but also on the liquid-to-gas density ratio. The PVC location can also be identified by the low pressure region which is shown by an arrow in Fig. 5(d). In Case A the lowest pressure region is in the core of the annular jet (Fig. 5(c)), as expected, showing the absence of the PVC. Positive intermediate magnitude axial velocity can be seen at the PVC location as indicated in Fig. 5(f). The maximum axial velocity occurs in curved regions indicated as A1 and A2. These curved regions are not evident in Case A where the maximum axial velocity appears to be evenly distributed around the jet column. This is due to the rather stable flow field in terms of vorticity observed in Case A, because of the reduced liquid-to-gas density ratio. Also, the PVC lies in between positive and negative $y-$ velocity regions as shown in Fig. 5(h).

Instantaneous streamwise velocity profiles at the jet centreline at different time instants are shown in Fig. 6. A large peak in the streamwise velocity is observed near the jet nozzle exit, due to the merging of the circular sheet of the annular jet. At the upstream locations before $z = 2.0$, the velocity profiles at different time instants are almost overlapping. The velocity field at the higher density ratio shows more significant spatial changes, indicating a more unstable flow field in comparison with the case with the lower density ratio. In Case A, shown in Fig. 6(a), the velocity profiles have negative values between $z = 1.25$ and $z = 1.85$, indicating the presence of a recirculation zone. The positioning of the recirculation zone is somewhat further downstream from the nozzle exit and thus such zone cannot be regarded as a GRZ. This zone is rather a central recirculation zone (CRZ) associated with swirling motion (Syred, 2006). The development of CRZ also occurs in Case B with its proximity ranging from $z = 1.35$ to $z = 2.50$. Further discussion regarding the CRZ and the GRZ development is given in the time-averaged flow properties. In both cases, after $z = 4.0$, velocity

fluctuations are present indicating the unsteady dynamic behaviour of the flow field. In Case B, the velocity fluctuations show more significant variations and form sharp peaks and troughs, indicating that this case is more vortical due to the promotion of the Kelvin–Helmholtz instability. The small velocity fluctuations present after $z = 7.0$, as shown in Fig. 6(b), indicate that the large-scale vortical structures have collapsed to smaller ones as it was also shown in Fig. 1(b). In Fig. 6, it is noticed that the large velocity peak near the jet nozzle exit of the lower density ratio case is much higher than that of the higher density ratio case, which is further discussed in Fig. 7.

5.2. Time-averaged flow properties

In an effort to better understand the physics behind the CRZ and the GRZ, and to further elucidate the effects of the liquid-to-gas density ratio on the flow development, time-averaged results are presented. The time interval used for the calculation of the averaging properties is between $t_1 = 23.3$ and $t_2 = 33.3$, after the flow has been developed. The time-averaged streamwise velocity contours in $y = 5.0$ plane are shown in Fig. 7. No vortical structures can be observed in the averaged results since they are an instantaneous flow feature. Case A shows no significant spreading until $z = 5.0$. After $z = 5.0$ the Kelvin–Helmholtz instability is established and causes the jet to spread more in the cross-streamwise direction. The cross-streamwise spreading occurs earlier in Case B and starts at around $z = 3.0$. A higher liquid-to-gas density ratio tends to increase the instability and thus the cross-streamwise spreading of the jet as shown by comparing Fig. 7(a) and (b).

The most important feature in Fig. 7 is the capturing of the CRZ and/or the GRZ, evident by the negative velocity regions represented by the dotted lines in the contour plots. In Case A both the GRZ and the CRZ are evident. The GRZ is positioned adjacent to the jet nozzle exit and it is a typical feature of annular jet flows (Sheen et al., 1996). In this cross-section, the GRZ has two branches on both sides of the jet centreline ($x = 5.0$). The existence of such a GRZ adjacent to the jet nozzle exit and around the jet centreline leads to an increase in the jet centreline velocity near the nozzle exit as shown in Fig. 6(a). The CRZ is positioned in between $z = 1.4$ and $z = 1.9$ and it is purely due to the swirling mechanism

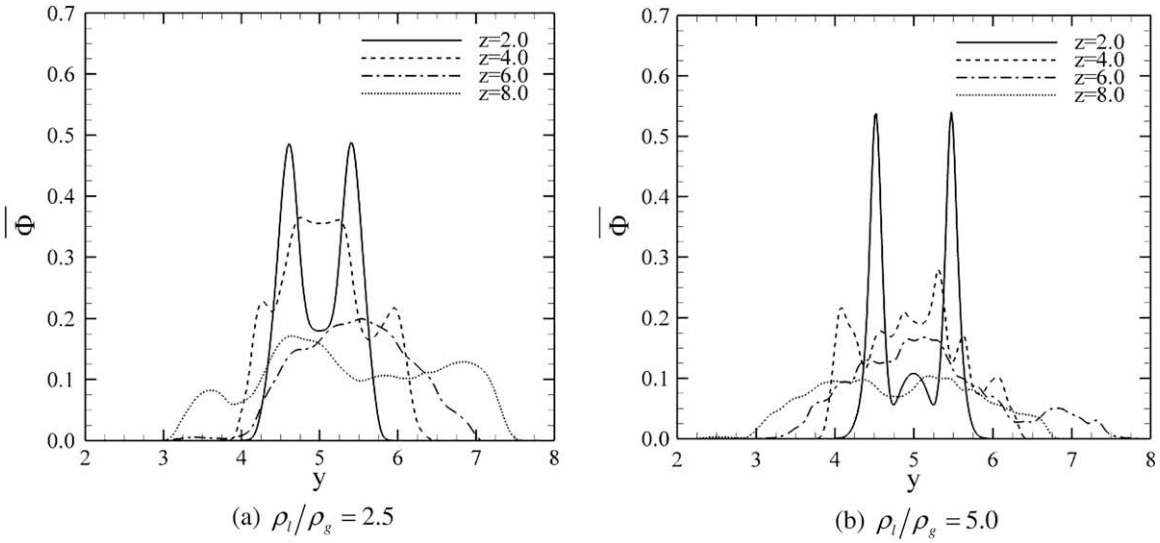

Fig. 8. Time-averaged liquid volume fraction profiles at different streamwise locations in $x = 5.0$ plane.

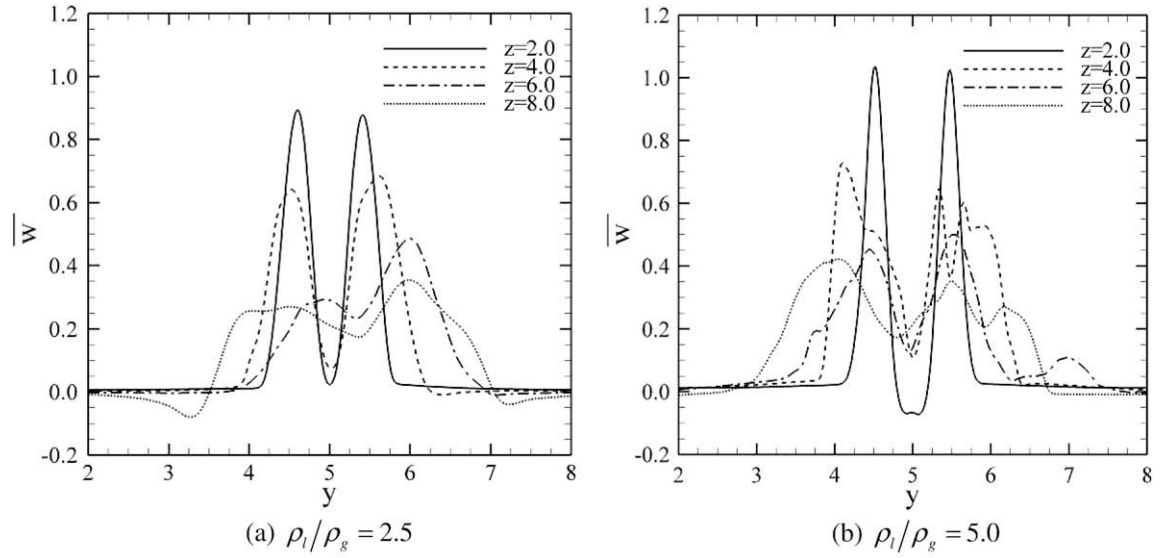

Fig. 9. Time-averaged streamwise velocity profiles at different streamwise locations in $x = 5.0$ plane.

(Syred, 2006; Lucca-Negro and O'Doherty, 2001; Sheen et al., 1996). It is noticeable that there is no GRZ formation in Case B and only a CRZ is evident lying in between $z = 1.25$ and $z = 2.5$. Although the two cases have the same moderate swirl number 0.4 (defined in terms of velocity only), the effects of swirl are more significant in the higher density ratio case due to the higher azimuthal momentum flux. Consequently, the higher density ratio case shows typical fluid dynamic behaviour of strong swirling jets such as the formation of CRZ and PVC (as indicated in Fig. 5). In the meantime, the GRZ which could possibly be formed immediately adjacent to the nozzle exit inside the annulus can be suppressed by the swirl due to the relatively large CRZ. On the contrary, the lower density ratio case shows the co-existence of GRZ and CRZ, due to the relatively weak swirling effects which are not able to suppress the GRZ and create the PVC but create only a weak CRZ. The existence of an annular "bell-shaped" GRZ next to the nozzle exit leads to the larger peak in the centreline velocity adjacent to the nozzle exit as shown in Fig. 6(a). It is known that the swirl number plays a significant role in the GRZ/CRZ interaction and PVC development (Jiang et al., 2008b) in single-phase jets. The two-phase flow results shown here indicated that under a certain swirl number, but different liquid-to-gas density ratios, the interaction between GRZ and CRZ can lead to different consequences. One of them may disappear and the GRZ/CRZ physics is highly dependent on the liquid-to-gas density ratio. The swirl number is no longer the only criterion which can satisfactory explain the physics behind the recirculation zones in the two-phase flow field.

Fig. 8 shows the time-averaged liquid volume fraction profiles at different streamwise locations in the plane of $x = 5.0$. In both cases, at $z = 2.0$, the liquid volume fraction profiles show similar profiles with two large branches and a deep crest. This is due to the jet annular configuration. For the higher density ratio case, the peak values of the two branches at $z = 2.0$ are higher than those for the lower density ratio case, which is due to the different velocity profiles of the two cases that dominate the dispersion of liquid. At further downstream locations, both cases show irregular liquid volume fraction distributions, indicating that the annular column has collapsed in between $z = 2.0$ and $z = 4.0$. In Case A, shown in Fig. 8(a), the liquid distribution shows increasing dispersion with decreasing magnitudes as the flow progress from upstream to further downstream locations. The same phenomenon is observed in Case B, with the only difference lying in the profiles at $z = 6.0$ and $z = 8.0$, which show relatively even distributions. At $z = 6.0$ the liquid volume fraction lies between $y = 3.0$ and $y = 7.5$, while at $z = 8.0$ the liquid volume fraction lies between $y = 2.3$ and $y = 6.8$. The liquid volume fraction magnitude shows decreasing values as the flow progress from $z = 2.0$ to $z = 8.0$, as expected. An important feature in Case B is the presence of a small peak at $y = 5.0$ ($z = 2.0$). This is due to the effects of the CRZ on the liquid distribution. Since $z = 2.0$ is at the heart of the CRZ (as shown in Fig. 7b), the velocity reversals associated with the CRZ tend to bring liquid from the outer side towards the inner core of the jet. This tendency is not present in Case A since the CRZ lies below $z = 2.0$, as indicated in Fig. 7(a).

Fig. 9 shows the time-averaged streamwise velocity profiles at different streamwise locations in the plane of $x = 5.0$. In both cases the profiles are very similar to the liquid volume fractions shown in Fig. 8. The negative velocity values at $z = 2.0$ in Case B, ranging from $y = 4.8$ to $y = 5.3$, are due to the presence of the CRZ in this region. Due to the existence of this recirculation zone, the two branches of the streamwise velocity at this location have higher peak values than those for the lower density ratio case. Both cases show decreasing velocity magnitudes at progressing downstream locations, due to the mixing of the annular jet with its ambient environment. The streamwise velocity profiles in Case B are more complex indicating an increased vorticity level in the flow field.

5.3. Results from POD analysis

POD analysis (described in Section 4.2) has been performed for the velocity fields in the time interval between $t_1 = 23.3$ and $t_2 = 33.3$, where instantaneous flow "snapshots" were analyzed. Tables 2–5 provide the normalized eigenvalues and their cumulative contribution to the fluctuating energy, in relation to the computational case, the individual velocity components and their corresponding 2D slices. From Tables 2–5 it is clear that, for the slices under consideration, 95% of the total energy which is the normal criterion used to judge the number of important modes in the flow field, can be captured in the first 10 POD modes, in both computational cases for both velocity components.

Fig. 10 shows the energy content and the corresponding fluctuating energy of the first 10 POD modes, for both velocity components (u, v), in various streamwise planes for the lower liquid-to-

Table 3
Normalized eigenvalues and their cumulative contributions to the fluctuating energy in various streamwise planes for the v-component of Case A ($\rho_l/\rho_g = 2.5$).

	$z = 2.0$		$z = 4.0$		$z = 6.0$		$z = 8.0$	
	λ_k	$\sum\lambda_k$	λ_k	$\sum\lambda_k$	λ_k	$\sum\lambda_k$	λ_k	$\sum\lambda_k$
1	59.814	59.814	48.773	48.773	30.472	30.472	68.422	68.422
2	32.577	92.391	28.540	77.312	20.643	51.115	16.463	84.885
3	5.759	98.149	4.553	81.865	15.267	66.382	6.071	90.956
4	0.675	98.824	3.670	85.536	9.959	76.341	3.825	94.781
5	0.414	99.238	3.148	88.684	7.627	83.968	1.393	96.174
6	0.367	99.606	2.772	91.455	5.175	89.143	1.284	97.458
7	0.130	99.736	1.910	93.365	3.107	92.251	0.926	98.384
8	0.064	99.799	1.668	95.033	1.670	93.921	0.482	98.866
9	0.043	99.842	0.964	95.997	1.372	95.293	0.381	99.247
10	0.031	99.873	0.800	96.796	1.219	96.512	0.212	99.459

Table 2
Normalized eigenvalues and their cumulative contributions to the fluctuating energy in various streamwise planes for the u-component of Case A ($\rho_l/\rho_g = 2.5$).

	$z = 2.0$		$z = 4.0$		$z = 6.0$		$z = 8.0$	
	λ_k	$\sum\lambda_k$	λ_k	$\sum\lambda_k$	λ_k	$\sum\lambda_k$	λ_k	$\sum\lambda_k$
1	61.889	61.889	44.115	44.115	30.530	30.530	42.177	42.177
2	24.067	85.956	26.990	71.105	27.402	57.932	34.480	76.657
3	13.047	99.003	5.575	76.680	11.363	69.294	10.026	86.683
4	0.447	99.450	5.395	82.076	7.809	77.103	4.527	91.210
5	0.189	99.639	3.964	86.040	7.394	84.497	3.414	94.624
6	0.168	99.807	3.572	89.611	4.538	89.036	1.687	96.311
7	0.078	99.885	2.572	92.183	2.734	91.770	0.974	97.285
8	0.047	99.932	1.832	94.015	2.019	93.789	0.837	98.122
9	0.024	99.955	0.983	94.999	1.679	95.467	0.655	98.778
10	0.016	99.971	0.869	95.868	1.069	96.537	0.315	99.093

Table 4
Normalized eigenvalues and their cumulative contributions to the fluctuating energy in various streamwise planes for the u-component of Case B ($\rho_l/\rho_g = 5.0$).

	$z = 2.0$		$z = 4.0$		$z = 6.0$		$z = 8.0$	
	λ_k	$\sum\lambda_k$	λ_k	$\sum\lambda_k$	λ_k	$\sum\lambda_k$	λ_k	$\sum\lambda_k$
1	57.528	57.528	39.561	39.561	22.219	22.219	47.380	47.380
2	26.786	84.314	31.407	70.968	17.851	40.069	17.280	64.660
3	13.817	98.131	8.511	79.479	15.442	55.511	10.676	75.335
4	1.091	99.222	5.624	85.104	8.306	63.817	7.233	82.569
5	0.364	99.586	2.862	87.965	7.148	70.965	4.286	86.855
6	0.149	99.735	2.164	90.129	6.056	77.021	2.769	89.624
7	0.086	99.821	1.864	91.994	4.365	81.386	2.382	92.006
8	0.068	99.889	1.341	93.335	3.604	84.989	1.487	93.493
9	0.051	99.941	0.930	94.265	2.997	87.986	1.362	94.855
10	0.022	99.963	0.727	94.992	2.382	90.368	1.121	95.976

Table 5
Normalized eigenvalues and their cumulative contributions to the fluctuating energy in various streamwise planes for the v-component of Case B ($\rho_l/\rho_g = 5.0$).

	$z = 2.0$		$z = 4.0$		$z = 6.0$		$z = 8.0$	
	λ_k	$\sum\lambda_k$	λ_k	$\sum\lambda_k$	λ_k	$\sum\lambda_k$	λ_k	$\sum\lambda_k$
1	60.514	60.514	46.659	46.659	21.640	21.640	46.880	46.880
2	27.909	88.422	23.320	69.979	15.606	37.246	21.068	67.948
3	9.231	97.653	9.957	79.936	12.311	49.558	8.326	76.275
4	1.443	99.096	6.488	86.424	10.201	59.759	6.545	82.820
5	0.343	99.439	3.099	89.523	8.984	68.743	4.985	87.805
6	0.186	99.624	1.803	91.326	7.489	76.232	2.901	90.706
7	0.142	99.767	1.685	93.011	4.494	80.727	2.035	92.741
8	0.096	99.863	1.276	94.287	2.997	83.724	1.367	94.107
9	0.067	99.930	1.002	95.289	2.581	86.305	1.185	95.292
10	0.025	99.955	0.590	95.879	2.374	88.679	1.062	96.354

gas density ratio case. In this figure, the "energy content" represents the contribution of an individual mode while "fluctuating energy" represents the cumulative contributions of the relevant modes. In Fig. 10(a), the first POD mode contains more than 61% of the total energy at $z = 2.0$. As the flow progresses to further downstream locations, the first mode energy content drops significantly (around 44% for $z = 4.0$ and around 30% for $z = 6.0$). At $z = 8.0$, the first mode captures around 42% of the energy which is more than that at $z = 6.0$, while modes 2 and 3 are also important. This is due to the development of the Kelvin–Helmholtz instability, causing the flow field to become rather unstable and thus more modes are involved in the energy content. The energy content at $z = 8.0$ does not follow the trend observed for other locations, due to the fact that the large scale structures in the flow field might have broken down into smaller ones, forming a more uniform flow field. For the v-component shown in Fig. 10(c) and (d), a noticeable observation is that the mode effects at $z = 8.0$ do not follow the general trend observed for other locations. Although the POD mode behaviour for the v-component is generally similar to that for the u-component, from Fig. 10(c) it is clear that the first mode at $z = 2.0$ captures less energy than its corresponding counterpart at $z = 8.0$, different from the trend for the u-component where at $z = 2.0$ the first mode captures more energy compared to the other z-slices. This is because of the two flapping modes applied at the jet nozzle exit, which affect the u-component and v-component of the velocity in different ways. The general trend in Fig. 10 is that the number of modes contributing to a certain amount of fluctuating energy increases at progressively downstream locations from $z = 2.0$ to $z = 6.0$. The exception occurs at $z = 8.0$, where the number of modes contributing to a certain amount of fluctuating energy is less than that at $z = 4.0$ and $z = 6.0$. This is due to the fact that the large scale structures may have broken down into smaller ones at $z = 8.0$, and consequently the flow is more uniform at this downstream location. The energy content and energy fluctuation of each mode are closely related to the topology of the flow vortical structures.

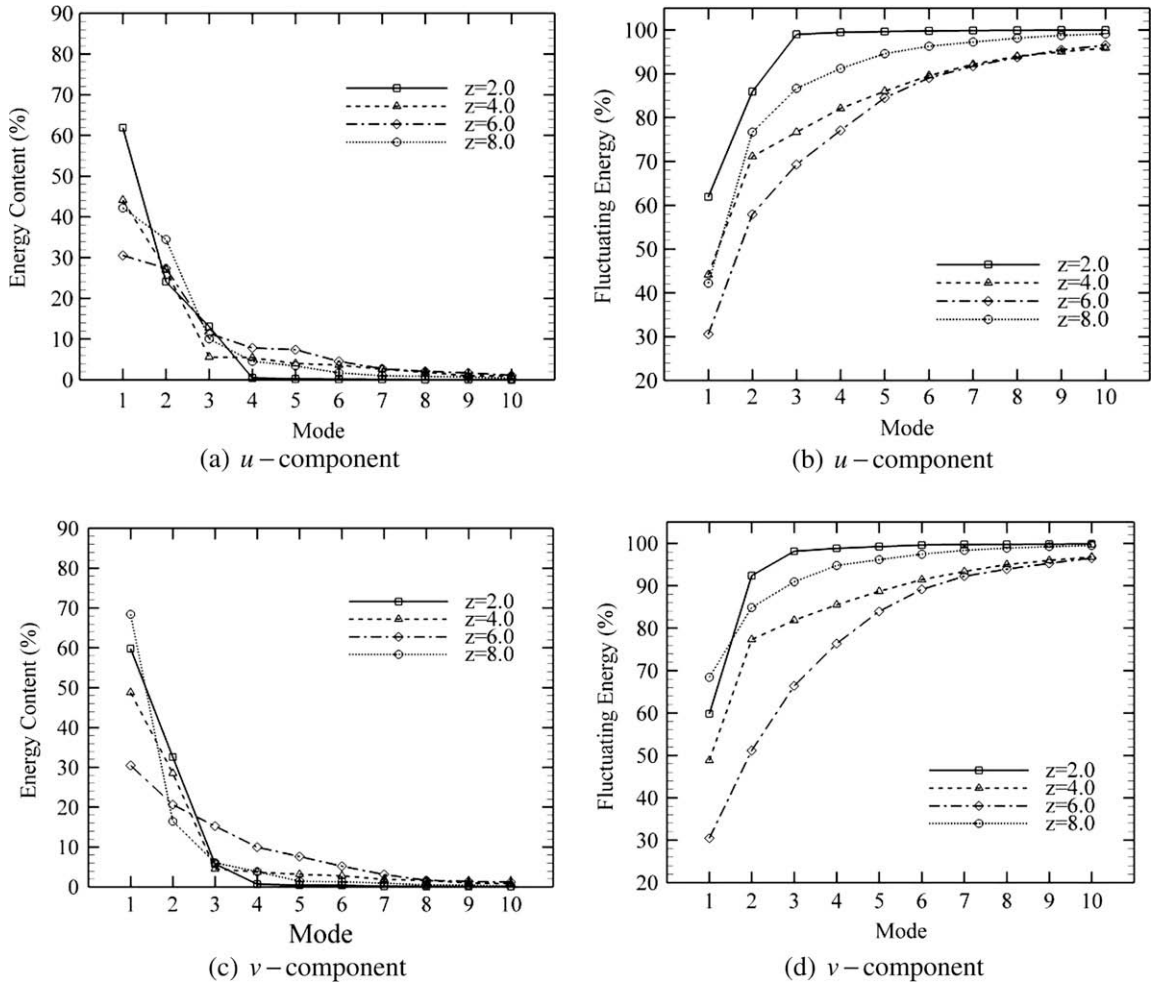

Fig. 10. Energy content and energy fluctuation of each POD mode for the two velocity components (u, v) of Case A ($\rho_l/\rho_g = 2.5$) in various streamwise planes, corresponding to velocity field at $t = 33.3$.

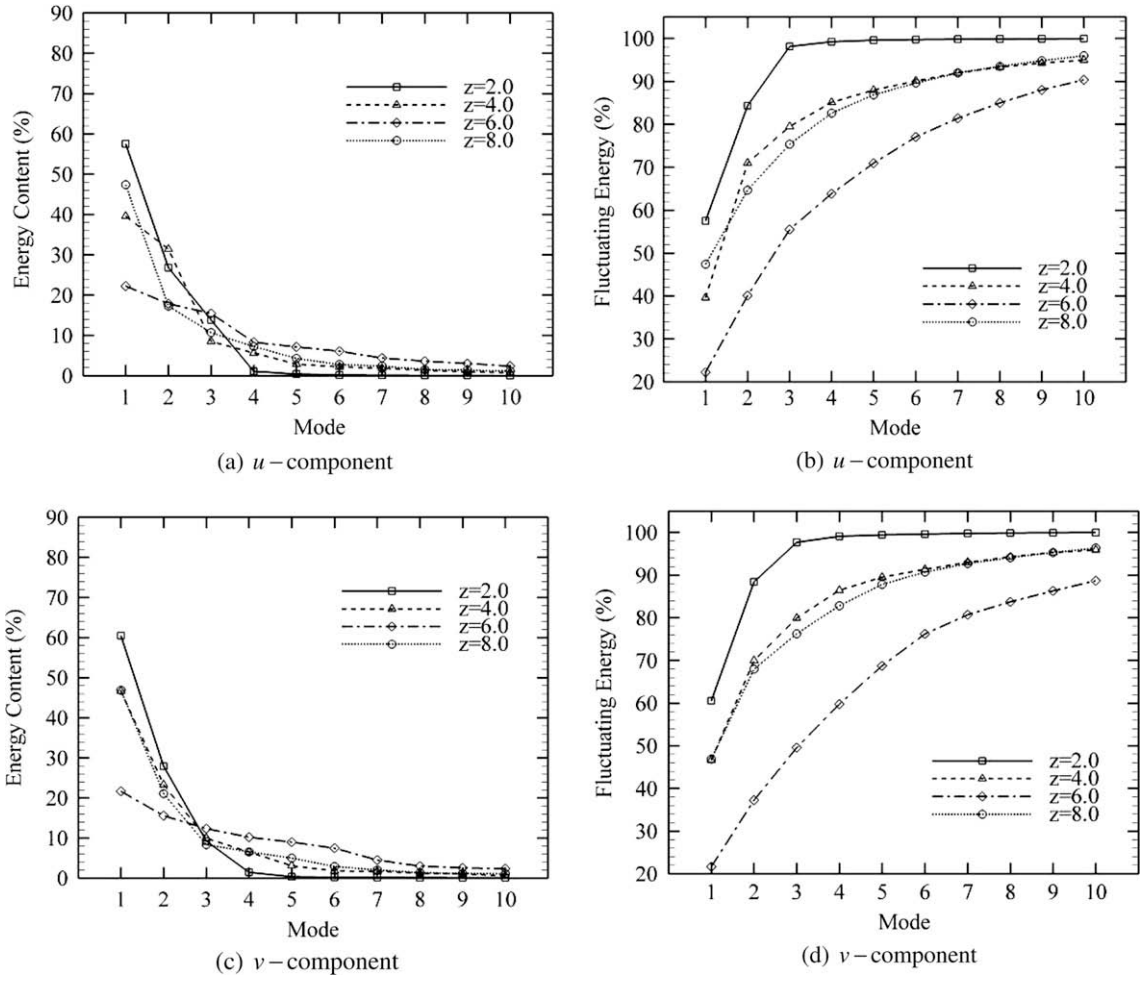

Fig. 11. Energy content and energy fluctuation of each POD mode for the two velocity components (u, v) of Case B ($\rho_l/\rho_g = 5.0$) in various streamwise planes, corresponding to velocity field at $t = 33.3$.

The energy content and energy fluctuation distributions for Case B are shown in Fig. 11. The general trend shown here for the higher density ratio case is consistent with that for the lower density ratio case. The most important comparison between Figs. 10 and 11 is that the percentage of the fluctuating energy of the higher density ratio case is generally lower than that of the lower density ratio case for a certain number of modes, indicating that a greater number of modes are of importance to the flow field at the higher density ratio. This is due to the fact that the flow field of the higher density ratio case is more unstable than that of the lower density ratio case.

POD analysis can be used to reconstruct the flow fields to illustrate the mode effects. Figs. 12 and 13 show such reconstructions. In Fig. 12, reconstructed velocity fields based on the first six most energetic POD modes are shown, for the cross-section $z = 6.0$ of Case A. It is evident that the POD modes extracted for $z = 6.0$ are very similar to each other indicating that the flow field is dominated by the first mode. More appreciable changes in the corresponding reconstructed velocity fields in Case B are evident, as shown in Fig. 13. Here the flow is significantly developed with the reconstructed velocity fields showing a gradual change with increasing mode number. The structural differences observed in Figs. 12 and 13 indicate the amount of energy captured by each mode. With increasing number of modes, the fluctuating energy also increases, with the reconstructed velocity field gradually approaching the DNS results. In Figs. 12 and 13, the topology of the flow vortical structures changes with the increase of mode number, indicating that the modes are closely related to the vortical structures.

6. Conclusions

The dynamics of annular gas–liquid two-phase swirling jets have been examined by DNS and POD. The three-dimensional, time-dependent, Navier–Stokes equations have been solved using highly accurate numerical methods. An Eulerian approach with mixed-fluid treatment combined with an adapted VOF formulation and a CSF model has been utilized to describe the two-phase flow system. Analytical equilibrium swirling inflow conditions have been used to generate the desired swirl level at the jet nozzle exit. Two computational cases have been performed, with relatively low and high liquid-to-gas density ratios, to examine density ratio effects on the flow field.

In both cases the flow field becomes more vortical at downstream locations with increasing liquid dispersion. It was identified that higher liquid-to-gas density ratio promotes the Kelvin–Helmholtz instability and thus the spatial liquid dispersion. The higher liquid-to-gas density ratio case is more vortical than the lower density ratio case. The POD results showed that 95% of the total fluctuating energy can be captured in the first 10 POD modes in both cases. For a certain number of modes, the percentage of the

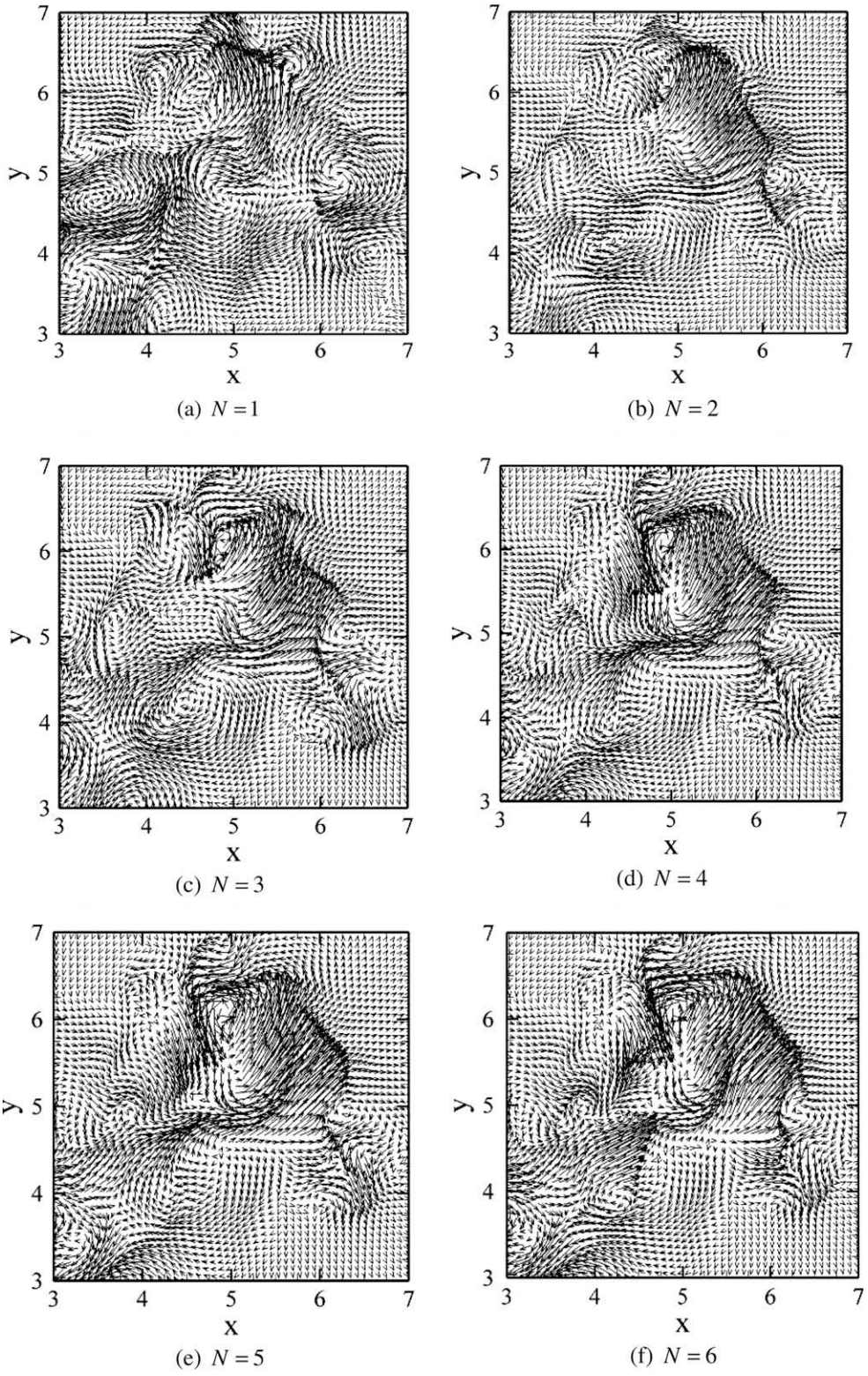

Fig. 12. Reconstructed velocity fields based on the first six most energetic POD modes in $z = 6.0$ for Case A ($\rho_l/\rho_g = 2.5$), corresponding to Fig. 4(c).

fluctuating energy of the higher density ratio case is generally less than that of the lower density ratio case, indicating that more modes are important to the flow field for high density ratio flows, revealing the rather unstable nature of the flow field. A future application of the POD method is to project the Navier–Stokes equations onto a finite set of POD eigenfunctions (Galerkin projection). This will reduce the flow description to a system of ordinary equations. The computational cost will be decreased while the flow physics may still be retained, which may also help linking the POD analysis with convective/absolute flow instability.

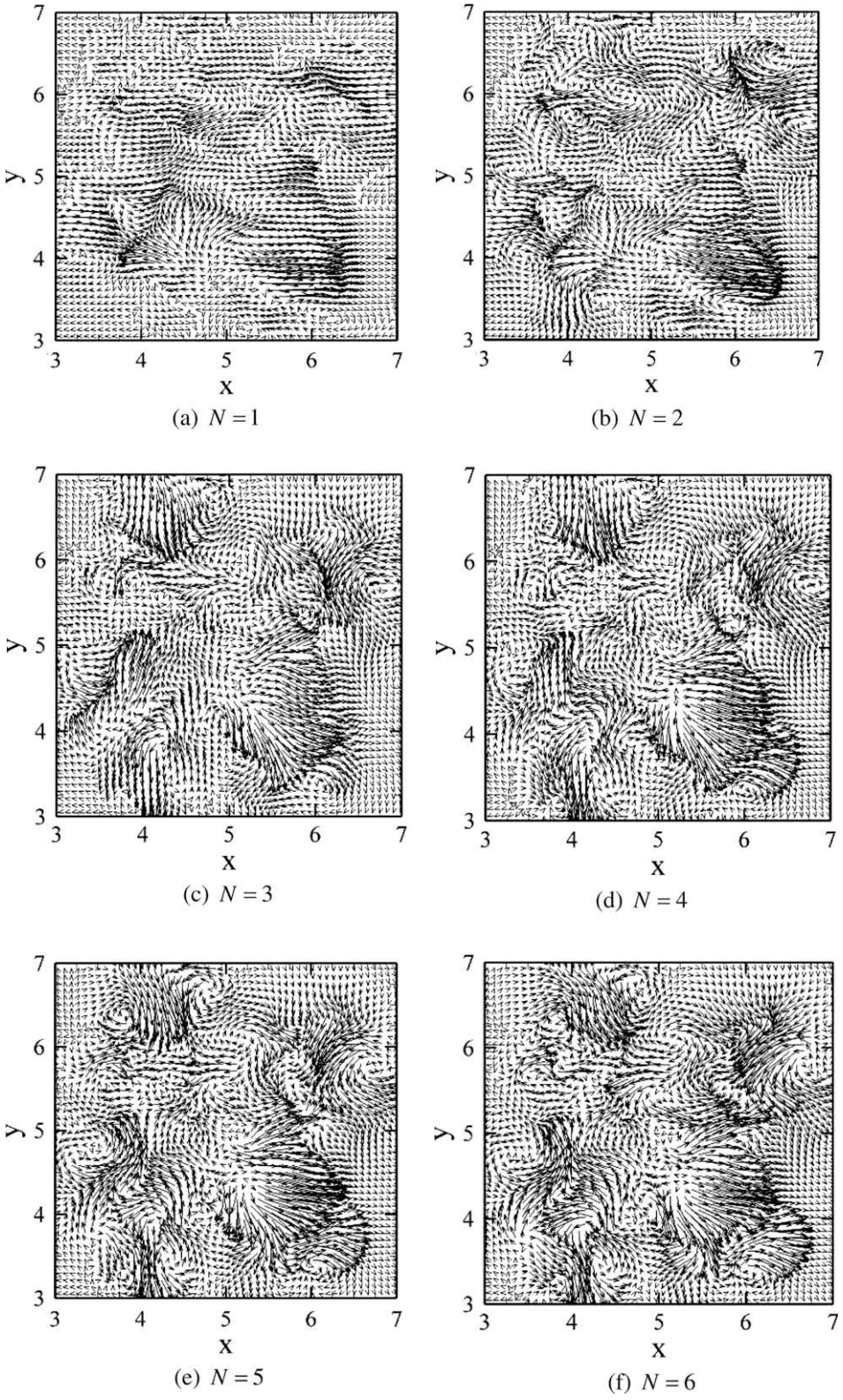

Fig. 13. Reconstructed velocity fields based on the first six most energetic POD modes in $z = 6.0$ for Case B ($\rho_l/\rho_g = 5.0$), corresponding to Fig. 4(d).

Useful physical insight has been gained from the simulations and the analysis of the results. In the lower density ratio case, two recirculation zones are identified: a GRZ adjacent to the jet nozzle exit due to the annular configuration, and a small CRZ located somewhat downstream of the GRZ. In the higher density ratio case, however, only one recirculation zone can be identified: a much larger CRZ located slightly downstream of the jet nozzle exit. Although the two cases have the same moderate swirl number, the effects of swirl are more significant in the higher density ratio case due to the higher azimuthal momentum flux. Closely related to the

CRZ, the DNS results indicate the formation of a PVC in the higher density ratio case. Consistent with experimental observations, it was shown that the PVC can exist in low swirl number flows. It was also shown that the swirl number alone is an insufficient criterion for PVC development in a two-phase flow since the PVC greatly depends on other inlet parameters such as the liquid-to-gas density ratio.

Finally, it needs to be noticed that, as a first step towards DNS of multiphase flow, interface reconstruction was not performed in this study. In order to capture the gas–liquid interface and the locations of the liquid phase, an interface reconstruction using the VOF-PLIC (piecewise linear interface calculation) method (Rider and Kothe, 1998) is currently underway. The VOF-PLIC method reconstructs the interface and thus allows visualization of liquid discontinuities and droplet formation. In addition, further variation of the liquid-to-gas density ratio, or Reynolds number, may be considered in the future to further investigate the PVC development and analyze the fine details of liquid disintegration. Other parameters such as the liquid-to-gas viscosity ratio may be examined to elucidate its effects in such complex two-phase flows but the excessive computational resources needed to perform such tests may prove to be prohibitive.

Acknowledgements

This work made use of the facilities of HPCx, the UK's national high-performance computing service. Computing resources were provided by the UK Turbulence Consortium (UKTC) under EPSRC Grant No. EP/D044073/1.

References

Adzic, M., Carvalho, I.S., Heitor, M.V., 2001. Visualisation of the disintegration of an annular liquid sheet in a coaxial airblast injector at low atomising air velocities. Opt. Diagnost. Eng. 5, 27–38.

Baik, S., Blanchard, J.P., Corradini, M.L., 2003. Development of micro-diesel injector nozzles via electromechanical systems technology and effects on spray characteristics. J. Eng. Gas Turb. Power 125, 343–427.

Banerjee, S., Lakehal, D., Fulgosi, M., 2004. Surface divergence models for scalar exchange between turbulent streams. Int. J. Multiphase Flow 30, 963–977.

Brackbill, J.U., Kothe, D.B., Zemach, C., 1992. A continuum method for modelling surface tension. J. Comput. Phys. 100, 335–354.

Chuech, S.G., 1993. Numerical simulation of nonswirling and swirling annular liquid jets. AIAA J. 31, 1022–1027.

Crowe, C.T., 2006. Multiphase Flow Handbook. Taylor & Francis, USA.

De Villiers, E., Gosman, A.D., Weller, H.G., 2004. Large Eddy Simulation of Primary Diesel Atomisation. SAE 2004-01-0100.

Del Taglia, C., Blum, L., Gass, J., Ventikos, Y., Poulikakos, D., 2004. Numerical and experimental investigation of an annular jet flow with large blockage. J. Fluid Eng. 126, 375–384.

Freitag, M., Klein, M., 2005. Direct numerical simulation of a recirculating, swirling flow. Flow Turbul. Combust. 75, 51–66.

Fulgosi, M., Lakehal, D., Banerjee, S., DeAngelis, V., 2003. Direct numerical simulation of turbulence in a sheared air–water flow with a deformable interface. J. Fluid Mech. 482, 319–345.

García-Villalba, M., Fröhlich, J., 2006. LES of a free annular swirling jet – dependence of coherent structures on a pilot jet and the level of swirl. Int. J. Heat Fluid Flow 27, 911–923.

García-Villalba, M., Fröhlich, J., Rodi, W., 2006. Identification and analysis of coherent structures in the near field of a turbulent unconfined annular swirling jet using large eddy simulation. Phys. Fluid 18, 055103/1–055103/17.

Gorokhovski, M., Hermann, M., 2008. Modeling primary atomization. Annu. Rev. Fluid Mech. 40, 343–366.

Gueyffier, D., Li, J., Nadim, A., Scardovelli, R., Zaleski, S., 1999. Volume-of-fluid interface tracking with smoothed surface stress methods for three-dimensional flows. J. Comput. Phys. 152, 423–456.

Gunes, H., Rist, U., 2004. Proper orthogonal decomposition reconstruction of a transitional boundary layer with and without control. Phys. Fluid 16, 2763–2784.

Gunes, H., Rist, U., 2007. Spatial resolution enhancement/smoothing of stereo-particle-image-velocimetry data using proper-orthogonal-decomposition-based and Kriging interpolation methods. Phys. Fluid 19, 64101/1–64101/19.

Gupta, K., Lilley, D.G., Syred, N., 1984. Swirl Flows. Abacus Press, Kent.

Hirt, C.W., Nichols, B.D., 1981. Volume of fluid (VOF) method for the dynamics of free boundaries. J. Comput. Phys. 39, 201–225.

Holmes, P., Lumley, J.L., Berkooz, G., 1998. Turbulence, Coherent Structures, Dynamical Systems and Symmetry. Springer, Cambridge.

Hübner, A.W., Tummers, M.J., Hanjalíc, K., van der Meer, Th.H., 2003. Experiments on a rotating-pipe swirl burner. Exp. Ther. Fluid Sci. 27, 481–489.

Hussain, A.K.M.F., Zaman, K.B.M.Q., 1981. The preferred mode of the axisymmetric jet. J. Fluid Mech. 110, 39–71.

Ibrahim, E.A., McKinney, T.R., 2006. Injection characteristics of non-swirling and swirling annular liquid sheets. Proc. Inst. Mech. Eng. C J. Mech. Eng. Sci. 220, 203–214.

Jakirlić, S., Hanjalić, K., Tropea, C., 2002. Modeling rotating and swirling turbulent flows: a perpetual challenge. AIAA J. 40, 1984–1996.

Jiang, X., Luo, K.H., 2000. Direct numerical simulation of the puffing phenomenon of an axisymmetric thermal plume. Theor. Comp. Fluid Dyn. 14, 55–74.

Jiang, X., Luo, K.H., 2003. Dynamics and structure of transitional buoyant jet diffusion flames with sidewall effects. Combust. Flame 133, 29–45.

Jiang, X., Luo, K.H., Siamas, G.A., 2008b. Swirling effects on the dynamics of an annular non-premixed jet flame. In: Proceedings of the 7th International ERCOFTAC Symposium on Engineering Modelling and Measurements (ETMM-7), Limassol, Cyprus, 4–6 June, pp. 798–803.

Jiang, X., Siamas, G.A., 2007. Direct computation of an annular liquid jet. J. Algo. Comput. Tech. 1, 103–125.

Jiang, X., Siamas, G.A., Wrobel, L.C., 2008a. Analytical equilibrium swirling inflow conditions for computational fluid dynamics. AIAA J. 46, 1015–1019.

Jiang, X., Zhao, H., Luo, K.H., 2007. Direct computation of perturbed impinging hot jets. Comput. Fluid 36, 259–272.

Klein, M., 2005. Direct numerical simulation of a spatially developing water sheet at moderate Reynolds number. Int. J. Heat Fluid Flow 26, 722–731.

Kollmann, W., Ooi, A.S.H., Chong, M.S., Soria, J., 2001. Direct numerical simulations of vortex breakdown in swirling jets. J. Turbul. 2. Art. No. N5.

Lele, S.K., 1992. Compact finite-difference schemes with spectral-like resolution. J. Comput. Phys. 103, 16–42.

Liao, Y., Jeng, S.M., Jog, M.A., Benjamin, M.A., 2000. Instability of an annular liquid sheet surrounded by swirling airstreams. AIAA J. 38, 453–460.

Lin, S.P., 2003. Breakup of Liquid Sheets and Jets. Cambridge University Press, Cambridge.

Lombardi, P., DeAngelis, V., Banerjee, S., 1996. Direct numerical simulation of near-interface turbulence in coupled gas–liquid flow. Phys. Fluid 8, 1643–1665.

Lucca-Negro, O., O'Doherty, T., 2001. Vortex breakdown: a review. Prog. Energy Combust. Sci. 27, 431–481.

Perry, R.H., Green, D.W., 1998. Perry's Chemical Engineers' Handbook. McGraw-Hill, Singapore.

Pierce, C.D., Moin, P., 1998. Method for generating equilibrium swirling inflow conditions. AIAA J. 36, 1325–1327.

Ramamurthi, K., Tharakan, T.J., 1998. Flow transition in swirled liquid sheets. AIAA J. 36, 420–427.

Rangel, R.H., Sirignano, W.A., 1988. Nonlinear growth of Kelvin–Helmholtz instability: effect of surface tension and density ratio. Phys. Fluid 31, 1845–1855.

Rider, W.J., Kothe, D.B., 1998. Reconstructing volume tracking. J. Comput. Phys. 141, 112–152.

Ruith, M.R., Meiburg, E., 2002. Direct numerical simulation of spatially developing, three-dimensional swirling jets. J. Turbul. 3. Art. No. N65.

Scardovelli, R., Zaleski, S., 1999. Direct numerical simulation of free-surface and interfacial flow. Annu. Rev. Fluid Mech. 31, 567–603.

Sheen, H.J., Chen, W.J., Jeng, S.Y., 1996. Recirculation zones of unconfined and confined annular swirling jets. AIAA J. 34, 572–579.

Shen, J., Li, X., 1996a. Breakup of annular viscous liquid jets in two gas streams. J. Propul. Power 12, 752–759.

Shen, J., Li, X., 1996b. Instability of an annular viscous liquid jet. Acta Mech. 114, 167–183.

Shen, J., Li, X., 2001. Absolute and convective instability of annular viscous liquid jets in gas streams. Atomization Sprays 11, 491–504.

Siamas, G.A., Jiang, X., Wrobel, L.C., 2008. A numerical study of an annular liquid jet in a compressible gas medium. Int. J. Multiphase Flow 34, 393–407.

Siamas, G.A., Jiang, X., 2007. Direct numerical simulation of a liquid sheet in a compressible gas stream in axisymmetric and planar configurations. Theor. Comput. Fluid Dyn. 21, 447–471.

Sirovich, L., 1987. Turbulence and the dynamics of coherent structures. Q. Appl. Math XLV, 561–570.

Sommerfeld, M., Qiu, H.-H., 1991. Detailed measurements in a swirling particulate two-phase flow by a phase-Doppler anemometer. Int. J. Heat Fluid Flow 12, 20–28.

Syred, N., 2006. A review of oscillation mechanisms and the role of the precessing vortex core (PVC) in swirl combustion systems. Prog. Energy Combust. Sci. 32, 93–161.

Thompson, K.W., 1987. Time dependent boundary conditions for hyperbolic systems. J. Comput. Phys. 68, 1–24.

Uchiyama, T., 2004. Three-dimensional vortex simulation of bubble dispersion in excited round jet. Chem. Eng. Sci. 59, 1403–1413.

Vanierschot, M., van den Bulck, E., 2007. Hysteresis in flow patterns in annular swirling jets. Exp. Therm. Fluid Sci. 31, 513–524.

Wang, M.R., Li, Z.X., 2004. Numerical simulations on performance of MEMS-based nozzles at moderate or low temperatures. Microfluid Nanofluid 1, 62–70.

Williamson, J.H., 1980. Low-storage Runge–Kutta schemes. J. Comput. Phys. 35, 1–24.

Wray, A.A., 1986. Very Low Storage Time-Advancement Schemes. Internal Report, NASA-Ames Research Center, Moffett Field, California.